

Accessing the Solid Electrolyte Interphase on Silicon Anodes for Lithium-ion Batteries *In-situ* through Transmission Soft X-ray Absorption Spectroscopy

Martin Schellenberger
Ronny Golnak
Wilson G. Quevedo Garzon
Sebastian Risse
Robert Seidel*

M. Schellenberger, W. G. Quevedo Garzon, R. Seidel
Department Operando Interfacial Photochemistry
Helmholtz-Zentrum Berlin für Materialien und Energie
14109 Berlin, Germany
E-Mail: robert.seidel@helmholtz-berlin.de

R. Golnak
Department Highly Sensitive X-ray Spectroscopy
Helmholtz-Zentrum Berlin für Materialien und Energie
14109 Berlin, Germany

S. Risse
Department Electrochemical Energy Storage
Helmholtz-Zentrum Berlin für Materialien und Energie
14109 Berlin, Germany

Keywords: solid electrolyte interphase, silicon anode, lithium-ion battery, in-situ, soft x-ray absorption spectroscopy

Abstract

Silicon offers nine times higher theoretical storage capacity than commercial graphite anodes for Li-ion batteries. For cycling stability, the electrolyte needs to be kinetically stabilized by the so-called Solid Electrolyte Interphase (SEI), a layer which ideally forms once from decomposition products of the electrolyte. While it works for graphite, the SEI on silicon fails to stabilize the electrolyte sufficiently, partly due to the large volume changes upon de-/lithiation. To investigate the SEI on silicon anodes, we developed a novel approach for X-ray Absorption Spectroscopy (XAS), that puts a twist to conventional SiN_x window-based liquid cells by utilizing a deliberately induced gas-bubble to form a soft X-ray transparent electrolyte layer. We demonstrate our approach to allow transmission XAS in the soft X-ray regime on liquids and electrode thin-film

materials under *in-situ* conditions. In our case XAS study of the SEI on silicon anodes, we reveal the main SEI constituents as Li acetate, Li ethylene di-carbonate or Li ethylene mono-carbonate, Li acetylacetonate, and LiOH. Additionally, we see evidence for aldehyde species which we attribute to possible liquid inclusions within a porous SEI morphology. We consider our method an appropriate tool for the successful engineering of a stable, efficient SEI in the future.

1. Introduction

With 3579 mAh g^{-1} , silicon offers a nine times higher theoretical storage capacity than graphite anodes, which dominate the current commercial Lithium-ion Battery (LIB) landscape [1], [2]. Being comparably cheap and earth-abundant, makes silicon a promising candidate to leverage LIB technology to meet ever increasing demands [2]. Unfortunately, up until now, silicon anodes suffer from severe capacity fading due to two reasons [1]. First, the incorporation of lithium into silicon is based on a conversion reaction. This uptake is accompanied by a volume expansion of up to 400%, and hence severe stresses lead to cracks and the loss of active material. Second, silicon anodes need to be operated in a potential range outside the thermodynamic stability window of commercially available organic electrolytes. Hence, the electrolyte needs to be kinetically stabilized by the SEI. The SEI is supposed to form during the first few charging cycles and presumably consists of in-/organic reduction products of the electrolyte [3], [4]. It stabilizes the electrolyte by suppressing the electron transfer, while still allowing the ion diffusion for the conversion reaction. While true for graphitic anodes, this appears to be not the case for silicon. Here, cracking continuously exposes unprotected electrode surface, leading to perpetual SEI growth. Even worse, research on silicon nanowires that show no pulverization but still suffer from severe capacity fading [5] suggests, that the SEI layer on silicon stabilizes the electrolyte insufficiently.

The properties of the SEI are expected to be determined by the interplay between the formed chemical species and their spatial arrangement [3]. However, due to its volatile nature and

inaccessibility, the picture of the SEI on graphite and especially silicon is very vague [6]. With a thickness of only 10 to 50 nm [4], [7]–[13], extracting sufficient amount of the SEI for subsequent mass spectroscopy is difficult [14]. Simultaneously, isolating the small SEI signal from the background, e.g. the underlying electrode material, is challenging for most spectroscopic methods. Additionally, lithium, fluorine, and organic compounds in the SEI are highly reactive and chemically volatile, thus, characterization of the SEI in its true, unaltered state is always challenging. Therefore, *in-situ* and *operando* approaches are necessary to gain a deeper understanding of the SEI.

Such *in-situ* and *operando* approaches are possible with X-ray Absorption Spectroscopy (XAS). In this study, we monitor the low-Z elements absorption edges contained in the SEI at the silicon L-edge between 95 and 140 eV, oxygen K-edge (520 – 555 eV), and fluorine K-edge (670 – 750 eV). XAS in the soft X-ray regime (sXAS) has been used before to investigate the SEI on LIBs electrodes [12], [15], [16] in *post mortem* and *ex-situ* studies, using fluorescent and electron yield techniques. However, these methods struggle with low signal to noise ratio, long counting times / high radiation dose, and electron yield is particularly susceptible to surface artefacts introduced by environmental exposure. XAS in transmission mode does not suffer from these drawbacks, but the small attenuation length of the soft X-ray radiation puts strong constraints on the experiment. While the SEI thickness of only 10 nm to 50 nm is ideal for X-ray transmission, its preparation and characterization are intricate, especially for *in-situ* conditions. The SEI is comprised of decomposition products of the electrolyte, hence an excess of the electrolyte must be present for a sufficient SEI to form, while this excess of electrolyte inevitably overshadows the SEI signal in a transmission measurement. In this work we present a novel approach to overcome this challenge. The experimental procedure is based on a microfluidic electrochemical half-cell with two soft X-ray transparent silicon nitride (SiN_x) membrane windows. The formation of bubbles in electrolytes under high intensity X-ray radiation has been a known problem inside this type of cells and

ultimately led to the wide adoption of flow cells. In this study, we use this to our advantage by removing excessive electrolyte through the controlled formation of a gas bubble. The individual steps of our approach are illustrated in Figure 1. After forming the SEI during cycling (B), we use a high intensity X-ray to create a gas bubble in the vicinity of the entrance window and push out excessive electrolyte from the probing volume (C). The bubble sits steadily in the center between the membranes and what is left in the beam path is a thin layer of electrolyte that covers the SEI and the anode. By using a low intensity X-ray to avoid beam damage, we can then investigate the SEI on silicon thin-film anodes *in-situ* through transmission sXAS, without the need to disassemble the cell and risk any environmental exposure (D).

Using 1M LiPF₆ in a 50:50 (v/v) mixture of ethylene carbonate (EC) and dimethyl carbonate (DMC) as a model electrolyte, we monitor the reduction of the organic solvent at the oxygen K-edge and the decomposition of the LiPF₆ salt at the fluorine K-edge. Changes in the silicon anode itself are investigated at the silicon L-edge. By comparing with the absorption spectra from reference compounds, we identify the forming species and study the SEI composition. This experimental procedure is the first step towards an indispensable tool for successfully engineering a stable SEI on silicon anodes.

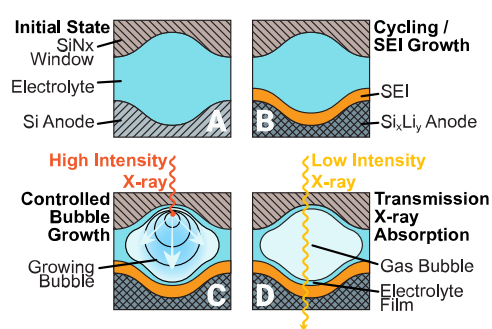


Figure 1: Illustration of our novel approach to investigate the SEI on silicon thin-film anodes in Li-ion batteries *in-situ* through transmission sXAS. **A:** The electrochemical cell for transmission sXAS consists of two silicon nitride membranes with an electrolyte channel in-between. The silicon thin-film anodes are deposited via plasma enhanced chemical vapor deposition onto the back-facing silicon nitride window (omitted in the illustration). **B:** The anodes are electrochemically cycled in a two-electrode setup, where the SEI forms on top of the then lithiated Si_xLi_y anodes. **C:** Through a high intensity X-ray beam a bubble is formed in a controlled manner to push away the excessive electrolyte. **D:** The SEI is investigated *in-situ* through transmission XAS with a low intensity X-ray to avoid any beam damage.

2. Results and Discussion

2.1. Cell Design and Bubble Formation

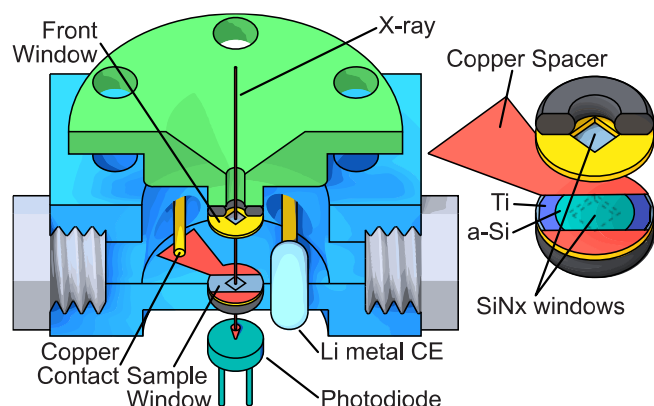


Figure 2: Sketch of the electrochemical cell for transmission sXAS. The cell consists of two PEEK parts: the lid (green) and the main body (blue). The silicon thin-film anode (teal) and an underlying titanium contacting layer (purple) are deposited onto a free-standing silicon nitride window (silver, side length 500 μm) in the center of a silicon frame (yellow, \varnothing 3 mm). The titanium contacting layer and in turn the anode are electrically contacted through the copper spacer (red). The copper spacer and a second silicon nitride window (yellow) form a sandwich assembly with an electrolyte channel in-between. This sandwich assembly sits in the center of the main body and is sealed by two O-rings (black) on each side. A small ribbon of lithium metal (light blue) acts as a counter-electrode (CE) and is placed 2 mm next to the sandwich assembly. Both the copper spacer and the lithium ribbon are contacted through a Kapton coated copper wire that is inserted into the cell through vacuum tight fittings on the back (not visible in the illustration). After assembly, the main body can be filled with electrolyte through two inserts (left and right) and sealed vacuum tight with two plugs (light grey). The X-ray enters the cell through the front window, penetrates the sample(-window) and its transmitted intensity is measured by a photodiode (teal).

We see our bubble approach as a novelty that allows the XAS investigation of conversion electrode materials for batteries through transmission in the soft X-ray regime under *in-situ* conditions. Like many other cell designs for transmission sXAS on liquids [17]–[21], our cell is based on a sandwich assembly of two silicon nitride (SiN_x) membrane windows, separated by a spacer to form a channel for the electrolyte. For our approach we chose commercially available (Micro to Nano V.O.F.), 50 nm thick, square SiN_x membrane windows with a side length of 500 μm in an octagonal silicon frame with a 3 mm diameter. The SiN_x membranes bulge outwards under vacuum [22] and the maximum membrane deflection at the center was calculated to be 23.5 μm . The calculation is given in the supplementary information (SI) under 1. *Calculation of the Membrane Deflection*. The volume that can be probed with the X-ray is referred to as the probing chamber in this work. Figure 2 shows a sketch of our cell design. The cell body (45 mm x 35 mm x 10 mm) and lid are machined out of PEEK (TECAPEEK, Ensinger GmbH). The membrane sandwich assembly sits in the center of the electrolyte reservoir, which is sealed from the

surrounding vacuum by the lid with two EPDM O-rings on each silicon frame. The electrolyte reservoir is 10 mm in diameter and 3 mm high. The total electrolyte volume of the cell is 0.23 mL, including all electrode channels. One SiN_x membrane (labelled as Sample Window in Figure 2) acts as the substrate for the 50 nm thick amorphous silicon thin-film anode, which is contacted by a 30 nm thick titanium layer underneath. The titanium layer is contacted via the copper spacer. The titanium was applied through evaporation and the silicon was deposited through plasma enhanced chemical vapor deposition. In the direction of the X-ray beam, the sample window sits on the back-facing side. This way, the formed SEI is shielded from the high intensity X-ray beam by the electrolyte during bubble creation. A thin ribbon of lithium metal is used as a counter-electrode and is placed outside of the beam path, about 0.5 mm away from the silicon frames. Both the lithium ribbon and the copper spacer are each contacted by copper wires. Before assembly, the whole cell and all components are thoroughly rinsed with methanol and dried with nitrogen. Afterwards the cell is assembled inside an argon glovebox (M. BRAUN, O₂ and H₂O kept <0.1 ppm) and sealed vacuum tight before the transfer to the experimental chamber at the beamline.

The idea to push away excessive electrolyte by forming a bubble was inspired by the work of Grogan *et al.*, who investigated the bubble formation in an aqueous electrolyte inside a similar cell under an electron beam in Transmission Electron Microscopy (TEM) [23]. They attributed the bubble formation to a continuously increasing concentration of dissolved O₂ and H₂ as radiolysis products. For high beam intensities they witnessed an explosive bubble formation that results in a large bubble sitting steadily in the center of the SiN_x membranes.

We adopt this principle to the radiolysis and heating of an organic electrolyte under high intensity X-ray radiation for our work. We propose that the bubble formation is governed by two converging mechanisms: an increasing concentration of dissolved gaseous radiolysis products and the heating of the electrolyte, which in turn lowers the gas solubility. When both quantities intersect,

the system is in a supersaturated state, the bubble nucleates and expands within the supersaturated electrolyte. We identified carbon monoxide CO and carbon dioxide CO₂ as the main decomposition gas species for the EC:DMC electrolyte. An extensive XAS study of the bubble gas with an in-depth discussion is attached in the SI under 3. *Bubble Gas Species Identification* with Figure S4.

We have developed a Finite Element Method simulation within the commercial COMSOL Multiphysics® software package [24] to understand the gas bubble formation better and perform the experiment procedure more reliably. The simulation first solves the diffusion and heat equation for the gas species concentration and the temperature inside the electrolyte with the beam acting as a mass and heat source. Then, the bubble growth is simulated by solving the Navier-Stokes equation in combination with a phase field approach to track the interface. Here, the bubble expansion is modelled in a quasi-empirical manner by connecting the continuity equation to the diffusion flux in the liquid/gas interface region. This approach is based on the work of Jafari *et al.* on the vapor bubble growth in a microchannel [25]. A description of the simulation is given in more detail in the SI under 11. *Beam Interaction and Bubble Simulation* with Figure S11, Figure S12, and Figure S13.

Figure 3 summarizes the simulation results assuming CO₂ as the sole radiolysis product and propylene carbonate (PC) as a simplified model electrolyte. The heat and the CO₂ concentration originate from the beam at $x = 0 \mu\text{m}$ and gradually spread throughout the cell with time. Due to the comparatively large thermal mass of the silicon frames (hatched areas in Figure 3a), the electrolyte temperature remains at 22 °C in the electrolyte channels adjacent to the frames and only increases within the probing chamber. In our experimental procedure, we first performed a preconditioning phase with a lower photon flux of $1 \cdot 10^{12} \text{ s}^{-1}$ to gradually increase the concentration throughout the cell without inducing the bubble, yet. Then, after 60 s to 90 s we increased the photon flux stepwise up to $7 \cdot 10^{12} \text{ s}^{-1}$ until the bubble is formed. The experimental bubble formation

procedure and the resulting dosage is discussed in detail in the SI under *4. Experimental Bubble Creation and Dosage Considerations* with Figure S5. For the simulation in Figure 3 the photon flux was increased from $1 \cdot 10^{12} \text{ s}^{-1}$ to $2.5 \cdot 10^{12} \text{ s}^{-1}$ at 90 s. Depending on the photon flux, the maximum temperature at $x = 0 \text{ }\mu\text{m}$ reaches a steady state plateau, while the concentration rises steadily (see Figure 3b). The solubility of CO_2 in PC decreases accordingly with increasing temperature. At the end of the preconditioning phase at 90 s we set the photon flux to a value of $2.5 \cdot 10^{12} \text{ s}^{-1}$, the solubility limit decreases, and the concentration increases rapidly. After 8 s, at 98 s total irradiation time, the solubility limit is exceeded at maximum temperature and concentration point. Taking oversaturation into account, we would expect bubble nucleation soon after. Figure 3e shows our experimental data of the dosage required to form the bubble (marked by the dot) of some representative samples, where changes in the slope correlate to changes in the photon flux. The preconditioning phase of 90 s is chosen in the simulation to match the two samples that are represented by blue and orange solid lines in Figure 3e. Here, we witness the bubble formation 5 s and 14 s after increasing the beam flux, which is in good agreement with our simulation result. However, we derive from Figure 3e a high variation in the dosage required for the bubble formation between samples. Based on our simulation, we attribute these variations to differences in the beam position relative to the probing chamber and to the resulting differences in the spatial distribution as well as in the maximum values for concentration and temperature. The challenge to position the beam reliably is discussed in the SI in more detail under *4. Experimental Bubble Creation and Dosage Considerations* with Figure S5.

Figure 3c shows the simulated bubble/electrolyte phase boundary at different points in time. It demonstrates how the bubble grows within the supersaturated electrolyte to reach its stable position in the center. The concentration above the solubility limit ($c - c_{\text{sol}}$) at an exemplary point in time is shown as the color surface plot in the background, and the corresponding bubble/electrolyte phase boundary is marked by the dashed line. Our simulation shows that the

gas bubble does not wet the boundaries for wetting angles larger than 120° , and a thin layer of electrolyte is left behind on both windows. We consider this bubble geometry to resemble a “plug/slug flow” (termed by Kawaji *et al.* [26]) similar to a gas-liquid flow in microchannels. This result matches the proposed model of Grogan *et al.* [23]. They demonstrated in their TEM experiment that the thin-film remains present through the continuous nucleation of gold nano particles from the electrolyte onto the SiN_x membranes by the electron beam. Figure 3d shows a post-mortem microscopic picture of an sXAS sample, which we have taken just after the sample had been removed from the vacuum chamber. The bubble outline can be seen in each corner. However, we assume that upon deflation of the membranes, the thin electrolyte layer gets disrupted into small islands, which can be seen by an iridescence pattern. The observed colorful iridescence pattern puts the actual electrolyte layer thickness in the sub micrometer range.

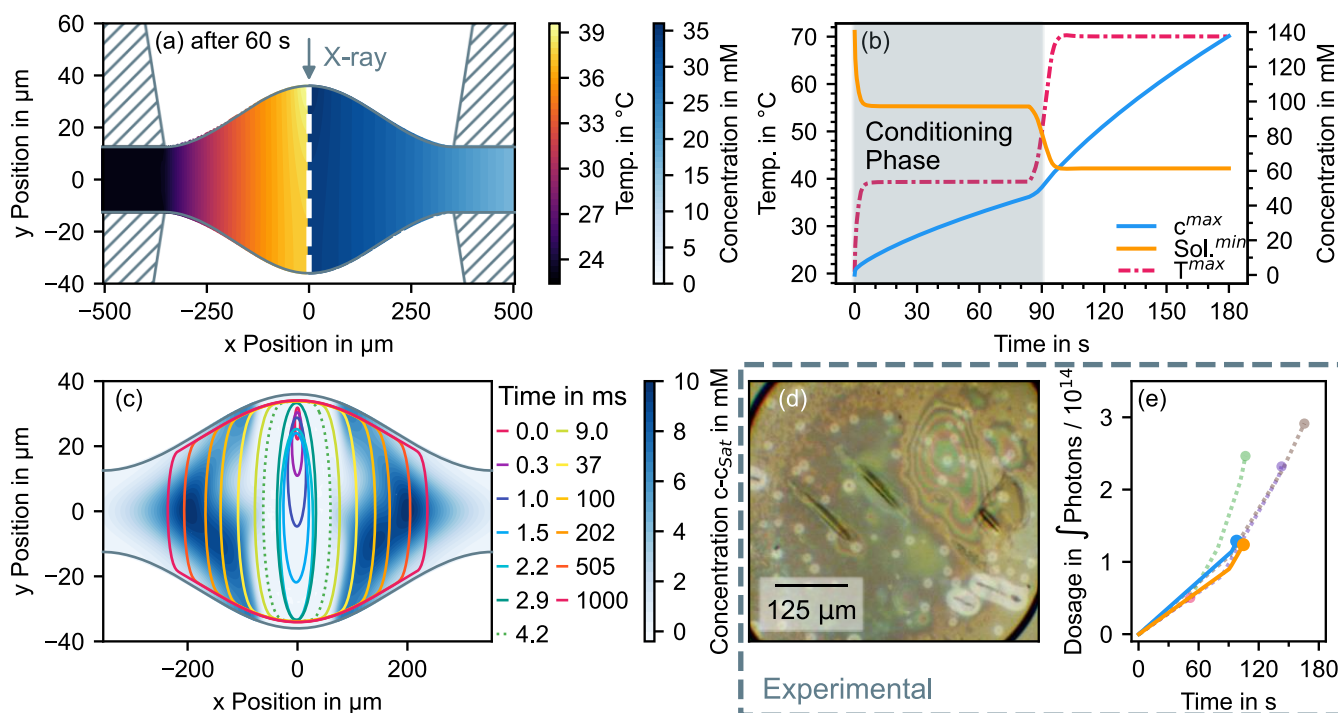


Figure 3: Beam interaction, bubble growth simulation, and experimental observations. (a) Spatial distribution of temperature (yellow/purple, left) and concentration (blueish, right) within the probing chamber after 60 s of beam exposure. (b) Maximum concentration and temperature within the probing chamber as function of time. Minimum solubility of CO_2 in neat PC as function of time, calculated based on maximum temperature. (c) Expanding phase boundary of the bubble/electrolyte, color coded by time. Color surface plot in the background correlates with the spatial distribution of the concentration above the solubility limit $c - c_{\text{sol}}$ at 4.2 ms and the corresponding phase boundary is highlighted by the dashed line. (d) Post-mortem optical microscopy pictures of sXAS cell right after removal from vacuum chamber. (e) Experimentally observed values of the dosage required to form the bubble.

2.2 Electrochemical and *Operando* UV/Vis Characterization

To create the SEI, the silicon thin-film anodes were cycled via linear sweep voltammetry (LSV), initially between the OCP at around 3.2 V and 10 mV vs. Li/Li⁺, and subsequently between 800 mV and 10 mV vs. Li/Li⁺. Between the lithiation and delithiation LSV, the anodes were potentiostatically held at 10 mV vs. Li/Li⁺ to facilitate the SEI formation. The holding was 100 s for the sample shown in Figure 4 and 1000 s for the *in-situ* samples (see **Table 2**). The current/potential curves of the initial, second, and 10th cycle of a representative 50 nm amorphous silicon thin-film anode in 1M LiPF₆ EC:DMC electrolyte with 100 s holding time at 10 mV vs. Li/Li⁺ are shown in Figure 4a. Judging the overall shape of the current-potential curves, the electrochemical behavior of the thin-films in our cell is in good agreement with reports on amorphous silicon thin-film anodes in simple “silicon in a beaker” and coin cell assemblies [27]–[35].

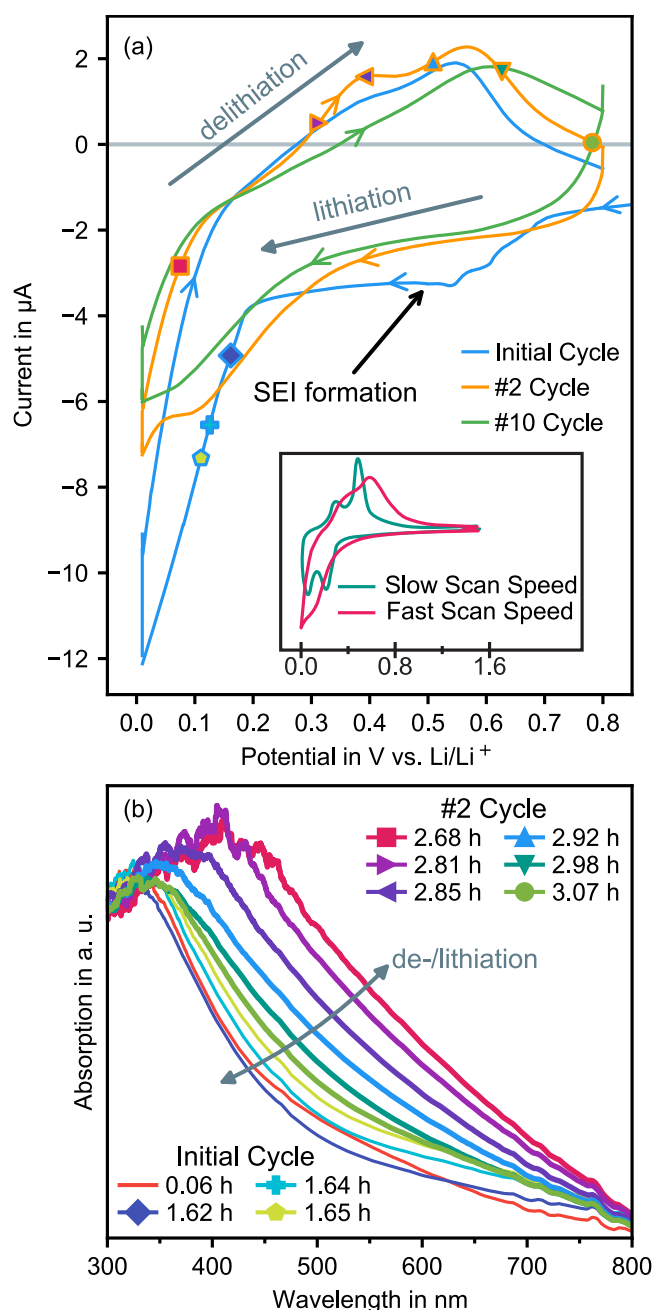


Figure 4: Electrochemical and UV/Vis characterization of the silicon thin-film anodes inside the sXAS cell. The electrochemical and UV/Vis data was obtained simultaneously. **(a)** I-U curves from the initial, second and 10th cycle. The symbols mark the points in time of the UV/Vis spectra in (b). The inset illustrates how the I-U curves transform for different scan speeds. The data is adapted from [27]. **(b)** Operando UV/Vis absorption spectra from the initial and second cycle.

In the lithium-silicon binary system, there are four phase equilibria: $\text{Si/Li}_{12}\text{Si}_7$, $\text{Li}_{12}\text{Si}_7/\text{Li}_7\text{Si}_3$, $\text{Li}_7\text{Si}_3/\text{Li}_{13}\text{Si}_4$ and $\text{Li}_{13}\text{Si}_4/\text{Li}_{21}\text{Si}_5$ [30], [36]–[38]. However, due to the kinetically hindrance by the high activation energy of Si-Si bond breaking, the equilibrium phases are not obtained at room temperature [39], [40]. Thus, the electrochemical lithiation of amorphous silicon (a-Si) proceeds via the formation of an amorphous, metastable, highly lithiated $\text{a-Li}_x\text{Si}$ phase [39], [41], [42]. The

a-Si/a-Li_xSi transformation is considered to be a solid-solution reaction, as indicated by a sloped dis-/charge profile in galvanostatic experiments. At room temperature, for potentials below 50 mV vs. Li/Li⁺, the a-Li_xSi phase further crystallizes into the terminal c-Li₁₅Si₄ phase via a two-phase reaction [39], [43], [44]. If the terminal c-Li₁₅Si₄ phase was obtained, the delithiation starts with the two-phase transformation to an a-Li_ySi phase ($y \approx 2$) first, which then proceeds to delithiated over the solid-solution back to a-Si* (* denotes a-Si after the first delithiation which presumably differs from the as-prepared a-Si, as discussed later in more detail). If the lithiation was limited to the a-Li_xSi phase in the first place, a-Li_xSi is delithiated through a solid-solution reaction back to a-Si* right away. The solid-solution a-Si/a-Li_xSi de-/lithiation takes place in two stages, as reflected by two distinguishable slopes or peaks in galvanostatic and potentiostatic experiments, respectively. The two distinguishable peaks during de-/lithiation in cyclic voltammetry are shown in the inset of Figure 4a. These two stages are presumably correlated to different local environments with higher and lower Li/Si coordination numbers at different Li content (further referred to as high- and low-potential stages) [39], [45]–[47]. Although the a-Si/a-Li_xSi transformations exhibit a sloped profile typical for solid-solution reactions, in their *in-situ* TEM studies, Wang *et al.* and McDowell *et al.* discovered a sharp phase boundary between the two phases for the initial lithiation of as-prepared a-Si, indicating a two-phase transformation not a solid-solution reaction [48], [49]. However, for the following delithiation as well as further lithiations, the phase boundary was not visible anymore. It was proposed that Si-Si bond breaking in as-prepared a-Si necessitates an increased Li content in its vicinity, which is only possible at a sharp phase boundary, but not at the forefront of a concentration gradient in a solid-solution. After the first delithiation however, the structure of a-Si* is altered to allow the lithiation in consecutive cycles through a solid-solution reaction. McDowell *et al.* [49] proposed possible differences between a-Si and a-Si* could be trapped residual Li content in the a-Si matrix as well as a less dense a-Si structure with more dangling bonds, which is indicated by a 25 % volume increase after the first cycle. Both changes may potentially facilitate recurring Li incorporation in consecutive cycles. In summary, the transformation from a-Si to a-Si*

is commonly observed as a unique dis-/charging behavior in the first cycle [39], [41], [42], [48]–[51].

As expected, looking at Figure 4a, the current/potential response of the initial cycle differs drastically from the consecutive cycles presumably due the structural changes from a-Si to a-Si*. On top of that, the initial cycle exhibits an overall higher anodic current with a pronounced plateau starting at 0.53 V vs. Li/Li⁺. An increased anodic current at potentials below 1 V vs. Li/Li⁺ in the initial cycle is common in literature and is correlated to the formation of the SEI [31], [52]–[56]. We assume the plateau is caused by the surface-limited electrolyte decomposition reaction on all electrode surfaces, i.e., the silicon thin-film itself as well as all copper contacting rods which are in contact with the electrolyte. In particular, Horowitz *et al.* correlated the plateau at 0.5 V to the specific reduction of EC to poly-EC and lithium ethylene di-carbonate [56].

Furthermore, in the initial cycle we observe a steep current increase at 190 mV, which can be correlated to the onset potential of the high-potential a-Si/a-Li_xSi lithiation stage. In literature, the onset potential in the initial cycle is reported to be around 200 to 220 mV vs. Li/Li⁺ [34], [57]–[60]. Further, the low-potential stage is not visible in the initial lithiation sweep. In the initial delithiation sweep, however, both low- and high-potential a-Li_xSi/a-Si delithiation stages are visible, albeit as broad convoluted peaks. After the initial cycle, the current/potential response of the silicon thin-films changes drastically. In the second cycle, the high-potential lithiation stage becomes visible as a small plateau at 80 mV and the onset of the low-potential stage can be suspected at 10 mV. We attribute the plateau character to the high contribution of the double layer capacity (compared to the rather small bulk lithiation process), which, simply put, distorts the current/potential curves by an anti-clockwise rotation, thus turning peaks into plateaus. Nevertheless, the low- and high-potential delithiation stages are apparent in the second sweep as distinctive peaks at around 390 mV and 570 mV vs. Li/Li⁺.

As it can be seen in the inset of Figure 4a (slow and fast correlate to 0.1 and 2.0 mV s⁻¹ based on the data of Xia *et al.* [27]), for high LSV scan speeds the de-/lithiation peaks broaden, convolute and shift to higher and lower potentials [61], respectively. Although we apply a rather slow scan speed of 0.5 mV s⁻¹, we already observe extensively broadened and convoluted peaks in Figure 4a. From this we deduce rather sluggish kinetics within our cell and attribute it to the thin electrolyte channel. Because the scan speed also shifts the peak positions, an estimation of the overpotential presumably introduced through the large distance between working and counter electrode (compare Figure 2) is difficult. The onset potential of the high-potential a-Si/a-Li_xSi lithiation stage in the initial cycle at 190 eV suggests an overpotential as large as 30 mV vs. Li/Li⁺, when compared to literature values [34], [57]–[60] between 200 to 220 mV vs. Li/Li⁺. Furthermore, although the lithiation was carried out down to 10 mV, we do not observe distinct peaks for the formation of the c-Li₁₅Si₄ phase. From this we infer that the cycling occurs between a-Si* and a-Li_xSi. Staying in the amorphous regime by avoiding the crystallization of c-Li₁₅Si₄ with an appropriate cutoff potential during lithiation is a common strategy to increase cycle stability of silicon anodes [47]. Based on this, we think our findings regarding the SEI on the silicon thin-film anodes investigated in this work is still relevant for their application. On top of that, with the SEI formation plateau in the initial cycle appearing already at 0.53 V vs. Li/Li⁺, we argue the estimated overpotential around 30 mV is not expected to change the SEI's composition drastically.

Additionally, we monitored the de-/lithiation of the thin-film anode through UV/Vis-Spectroscopy (UV/Vis). UV/Vis absorption spectra recorded simultaneously at different times during the initial and second cycle are shown in Figure 4b. The corresponding symbol in Figure 4a marks the point in time of each absorption spectrum. The UV/Vis absorption evolution follows the current/potential response and changes continuously with the degree of lithiation. For a higher degree of lithiation, the absorption increases in the whole measured spectral region from 300 nm to 800 nm, and the absorption maximum moves from 350 nm to 400 nm. However, like the current/potential response,

the initial cycle differs from the other cycles. The UV/Vis absorption changes rapidly during the initial lithiation of amorphous silicon (see 1.62 h, 1.64 h, and 1.65 h in Figure 4b). For all consecutive cycles, the absorption continues the behavior of the second cycle. We suggest the changes during the initial cycle correlate to the breaking open of the silicon structure with an increasing degree of dangling bonds, similar to the structural changes from a-Si to a-Si*. By comparing the initial pristine absorption spectrum (0.06 h) with spectra after the initial cycle, we observe that the silicon thin-films are not fully transformed back to their pristine state. We attribute this to the expected a-Si/a-Si* structural changes. We propose that the overall slight increase in UV/Vis absorption may hint at trapped residual Li content as suggested by McDowell *et al.* [49]. Furthermore, the continuous change in the UV/Vis absorption confirms our claim that the silicon thin-films remain in the amorphous regime and the cycling takes place between a-Si* and a-Li_xSi. Thus, we assign the spectra of the higher lithiated (red square, 2.68 h) and lower lithiated state (green circle, 3.07 h) to a-Si* and a-Li_xSi, respectively. The extended dataset of the UV/Vis and electrochemical data from Figure 4 for the first 11 cycles (out of 20 total) is shown in Figure S6.

2.3. X-ray Absorption Spectroscopy

2.3.1. Oxygen K-Edge

Electrolyte and the "Thickness Effect"

After the bubble is created, the electrolyte remains a thin layer on top of the SEI (Figure 1, Figure 3c,d). In a first step, we will investigate the pure electrolyte by transmission sXAS. We will also address the "Thickness Effect" as a significant intrinsic challenge requiring cautious interpretation of the obtain absorption spectra.

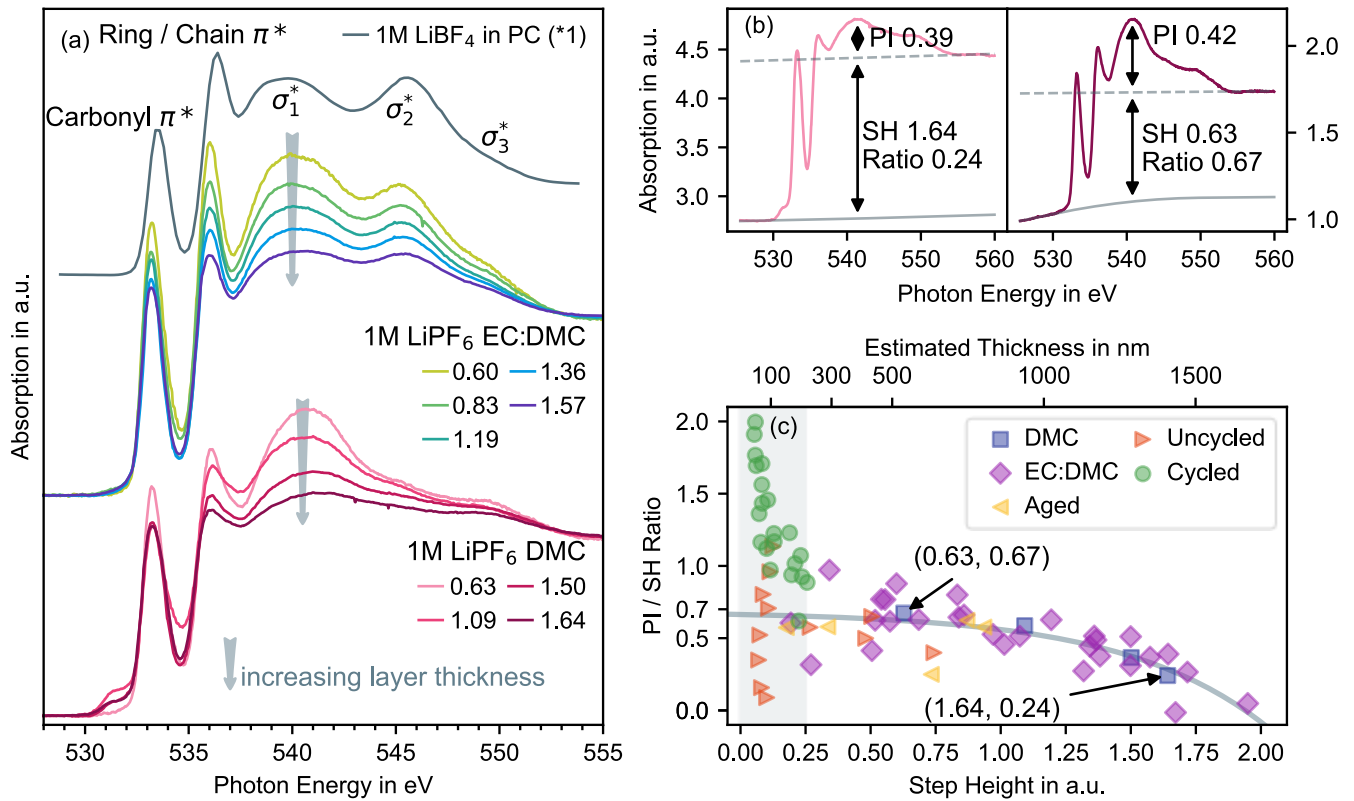


Figure 5: Transmission sXAS spectra at the oxygen K-edge. **(a)** 1M LiPF₆ in DMC and EC:DMC together with 1M LiBF₄ in PC for comparison (*1 from [62]) - Demonstration of the “Thickness Effect”: 1M LiPF₆ in DMC and EC:DMC at different sample positions that exhibit a different Step Height (SH) prior to the normalization to a common SH. **(b)** Demonstration of the applied adaptive background procedure and the determination of the SH and Peak Intensity (PI) in the raw data of two representative measurements of 1M LiPF₆ in DMC. The values of the shown spectra are marked in (c). **(c)** Quantification of the “Thickness Effect”: Correlation between the PI/SH ratio and the SH for 1M LiPF₆ in DMC and EC:DMC and aged, uncycled and cycled samples. A total thickness is estimated through the SH and given as secondary axis. The line is a fit of the data from DMC and EC:DMC to (1) and shown as a visual aid without physical reasoning of the fitting parameters.

The oxygen K-edge absorption spectra of 1M LiPF₆ in DMC and EC:DMC are shown in Figure 5a for different step height (SH) values. The SH value and how it can be correlated to the electrolyte layer thickness is discussed in more detail below and the “1M LiPF₆” specification is omitted in the following discussion. The EC:DMC absorption spectrum exhibits two sharp features at 533.27 eV and 536.06 eV photon energy and three broader peaks beyond the ionization edge at around 540 eV, 545.5 eV and 550 eV. To our knowledge, no XAS data on the EC:DMC system is available in the literature yet. However, the absorption spectra can be explained in analogy to the liquid microjet characterization by Smith *et al.* on a similar system, LiBF₄ in PC, where the individual absorption peaks were correlated to energetic isosurfaces in a density functional theory simulation [63]. The oxygen K-edge absorption spectrum of 1M LiBF₄ in PC from this study is shown in Figure

5a for comparison. Given the different chemical structure of PC and EC:DMC, the spectra is shifted to lower photon energy by about 0.5 eV, but the overall spectral shape is identical.

Based on the work of Smith *et al.*, the sharp peak in the pre-edge region at 533.27 eV correlates with the core 1s to π^* transition from the carbonyl oxygen atom. The influence of the chemical backbone on the core 1s to π^* transition of the carbonyl functional group was demonstrated by Urquhart *et al.* [64]. Thus, a shift by about 0.5 eV from PC to EC:DMC is expected. In the same way, the 1s to π^* transition from the oxygen atom in the ring structure of EC and the chain structure of DMC is attributed to the sharp peak at 536.06 eV. In the post-ionization edge region, the broad features σ_1^* , σ_2^* and σ_3^* correlate to the core-1s-to- σ^* -transitions. According to Smith *et al.*, in case of PC, the spectral intensity of these features cannot be allocated to a specific oxygen site. However, comparing the peak intensities of DMC to EC:DMC, it is apparent that the σ_2^* peak stems from the oxygen in the EC ring structure. Absorption spectra of the neat electrolyte components EC and DMC together with the spectral changes upon mixing and salt addition are discussed in more detail in the SI under 8. *Electrolyte Oxygen K-edge X-ray Absorption Spectroscopy* and Figure S8.

While free of self-absorption, saturation effects or decay path yields, the spectral shape obtained from transmission XAS measurements still depends on the sample thickness. This was first described by Parratt *et al.* in 1957, and it was named the “Thickness Effect” [65]–[69]. This effect was attributed to the spectral window of the detector, which leaks flux with higher and lower energy compared to the set photon energy [65]. While this explanation was given for a two-crystal X-ray spectrometer paired with a continuous X-ray source, our case of a non-energy-dispersive photodiode paired with monochromatized synchrotron radiation is analogous to it. In our case, the spectral window of the detector is replaced by the energy distribution (e.g., Gaussian or Lorentzian) of the monochromatized incoming flux [70]. The non-energy-dispersive photodiode then always registers a photon flux that is the convolution of the true transmission function of the

sample with the energy distribution of the incoming beam. In the recorded absorption spectrum, this convolution leads to a “washing out” of the maxima and minima and is notably dominant in the vicinity of absorption peaks and valleys. Furthermore, this influence of the leaking flux is more pronounced for thicker samples, hence the name “Thickness Effect”.

To distinguish the SEI from the covering electrolyte layer we need to know how the electrolyte spectrum evolves with its thickness. Hence, we need to quantify the “Thickness Effect”. From Figure 5a, we observe a washing out in the ring/chain π^* and in the σ_1^* peak of DMC and EC:DMC. We also observe a relative intensity decrease with increasing layer thickness. As the electrolyte-layer thickness is not accessible experimentally, we use the SH (before normalization), which is generally considered a measurement of how many atoms are inside the beam path [71], [72]. In Figure 5c, we give a rough estimated thickness, based on an overall linear attenuation coefficient for EC:DMC with an overall composition of $C_3H_5O_3$ and a density of 1.30 g cm^{-3} [73], [74]. The estimation of the thickness is described in more detail in the SI under 7. *Thickness Estimation at the Oxygen K-edge* and Figure S7. As proposed by Parratt *et al.*, we use the ratio between the intensity of the highest peak (PI) to the step height (SH) to quantify the degree of “washing out”. The determination of the SH and PI are illustrated in Figure 5b. According to Parratt *et al.*, this ratio converges for thinner samples towards a value that resembles the true absorption for an infinite thin sample. For smaller SH the PI/SH ratio of DMC and EC:DMC appears to converge to a value of around 0.7. The line given in Figure 5c is a fit of (1) to the datapoints of EC:DMC, where \mathcal{H} is the PI/SH ratio, ζ is the SH, and A , B , C , and D are fit-parameters without physical meaning.

$$\mathcal{H} = A \exp\left(\frac{\zeta - B}{C}\right) + D \quad (1)$$

We intentionally picked areas where the SEI appears to be covered only by a thin layer of electrolyte based on the transmission signal strength for our *in-situ* samples. With the SEI itself expected to be only a few nanometers thick, these measurements conclusively have an SH below 0.25, as shown in Figure 5c. At the same time, these samples exhibit PI/SH ratios ranging from 1

to 2. However, we would not expect such high values from the electrolyte itself, even when taking the “Thickness Effect” into account and extrapolating it to an infinitely thin layer. From Figure 5c we can deduce SEI species' presence by comparing our cycled cells to the uncycled ones and the electrolyte. In the following we compare the individual XAS spectra and isolate the SEI spectrum by adept subtraction.

Characterization of Solid Electrolyte Interphase

Extracting the Transmission Spectrum of the Solid Electrolyte Interphase

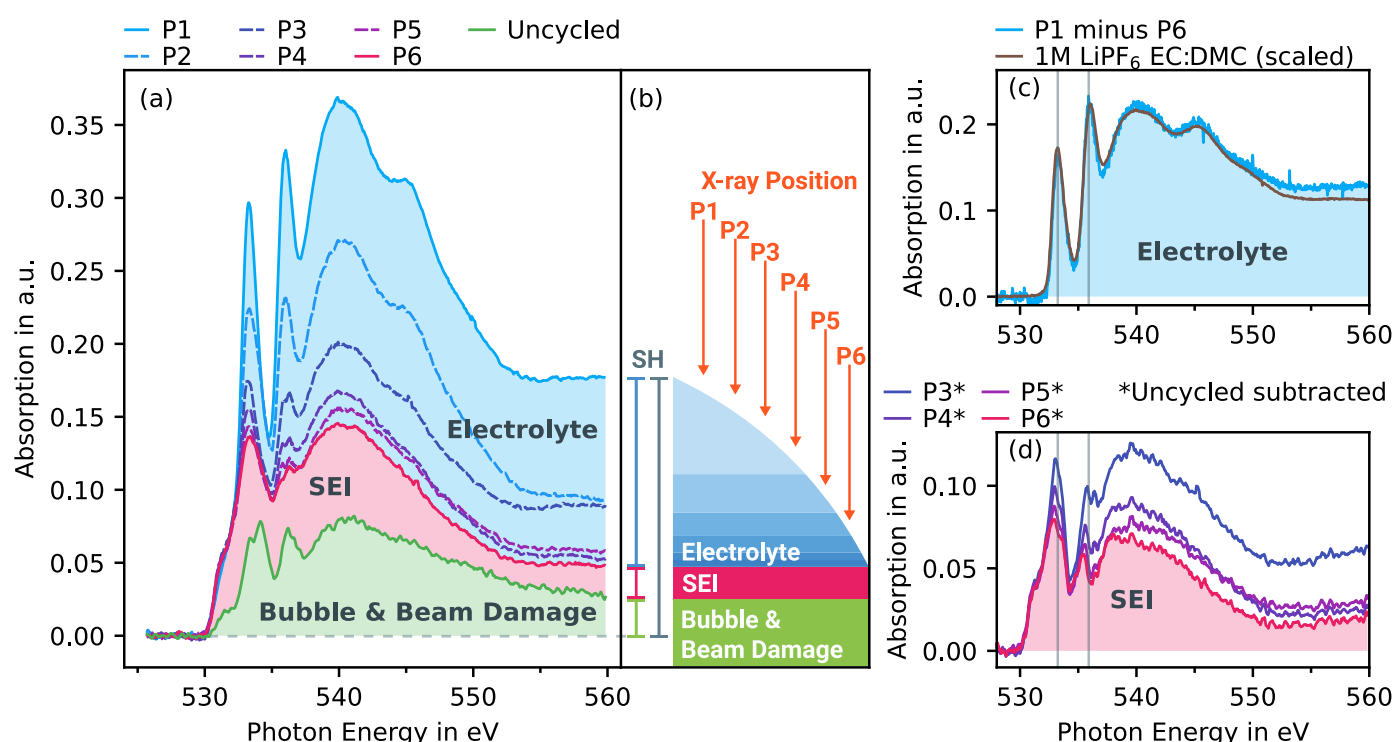


Figure 6: Extraction of the SEI spectrum from the overshadowing electrolyte spectrum and subtraction of the bubble and beam damage. **(a)** Oxygen K-edge transmission sXAS spectra of cycled cells at six different sample positions P1 to P6 alongside one spectrum of an uncycled cell. The blue background represents the contribution of the overlying electrolyte, red for the SEI, and green represents the bubble and beam damage. **(b)** Illustration of the individual spectral contributions from (a) in a layer scheme: the bubble and beam damage form the background of the spectrum, the SEI has a constant contribution throughout the whole sample (P1 to P6) as indicated by the constant shoulder at 531 eV and depending on the sample position the electrolyte has varying thickness where the spectral contribution decreasing accordingly from P1 to P6. **(c)** Isolation of the electrolyte spectrum that sits on top of the SEI by subtracting P6 from P1. For comparison a spectrum of 1M LiPF₆ in EC:DMC with a SH of 0.60 is scaled to 19% and shown alongside the isolated electrolyte spectrum. **(d)** Isolation of the SEI spectrum by subtracting the uncycled spectrum from P3 to P6.

To isolate the SEI spectrum, we refrain from normalization and take the absorption values as measured without normalization. This way, we can treat the obtained spectra as a linear combination of all individual chemical species within the beam path. By an adept comparison of

the spectra, we can then distinguish the individual contributions. Figure 6a shows absorption spectra at the oxygen K-edge from a cycled sample at six different positions (P1 to P6) that exhibit different step heights. Between P1 and P6 the overall spectral shape varies drastically, except for a small shoulder at 531 eV. This shoulder indicates the presence of a uniform SEI layer that is present throughout the cycled samples and absent on the uncycled one. Simultaneously, we attribute the change in the SH to the varying amounts of the electrolyte on top of the SEI. It must be noted that the uniformity refers to the SEI layer being present with comparable thickness at every sample position. The SEI layer in itself might be inhomogeneous as we will discuss later in more detail.

Consequently, for P1 with the highest SH, the thick electrolyte layer overshadows the SEI entirely, and the overall spectral shape appears to match the electrolyte. In contrast, at positions P2 to P6 with a more minor SH, less electrolyte is present, and the spectral shape of the SEI is revealed more and more. This interpretation is illustrated in Figure 6b, where the different positions P1 to P6 refer to locations with different electrolyte layer thicknesses. This can be confirmed by subtracting P6 from P1. The corresponding difference spectrum is shown in Figure 6c and matches an electrolyte spectrum of 1M LiPF₆ in EC:DMC. The measured electrolyte reference spectrum has an SH of 0.6 and was multiplied by a factor of 0.19. The extracted electrolyte spectrum P1 minus P6 has an SH of roughly 0.13, which correlates to an estimated electrolyte thickness of about 112 nm (see Figure 5c). The matching spectra with SH 0.6 and 0.13 back up our assumption that the “Thickness Effect” becomes negligible for smaller SH and that the electrolyte spectrum with SH 0.6 already resembles the true spectral shape at a reasonable degree.

So far, we only distinguished the electrolyte contributions in our spectral data, and we can refine the fingerprints of the SEI even further. As discussed before, the gas bubble contains gaseous oxygen species and to create the bubble beam damage was induced to the electrolyte by the high

intensity X-ray. As illustrated in Figure 6b (“Bubble & Beam Damage”), we take both contributions (gas species and radiolysis products left in the electrolyte still covering the SEI) as an underlying background and obtain this data experimentally from the uncycled sample. Consequently, differences between the uncycled and cycled spectra are directly correlated to the electrochemically induced SEI formation. The corresponding difference spectra are shown in Figure 6d. From our experimental data it is straightforward that P6 is the spectrum with the smallest electrolyte contribution and hence with the most dominant SEI signal. We refer to the corresponding difference spectrum P6* from Figure 6d as the SEI spectrum and discuss it in more detail in the next chapter. It must be noted that the individual contribution of the electrolyte in P6 and the uncycled spectrum is intrinsically unknown. Hence, we expect the extracted SEI spectrum still to contain the electrolyte signal to a minor degree.

At this point we want to mention that we consider any beam damage of the SEI itself during bubble creation by the high intensity X-ray highly unlikely. The silicon anode and the SEI are located on the back facing SiN_x window and both are shielded by the full thickness of the electrolyte (72 μm). Figure S12 in the SI demonstrates the efficiency of this shielding by showing how quickly the photon density decays completely within 10 μm of the electrolyte. As a further precaution, we exclude the beam position of the bubble creation from further XAS measurements, to rule out any beam damage contribution. As for potential beam damage of the SEI during XAS itself, based on the extremely low beam intensity, we estimated the expected mole fractions of potential radiolysis products to be uncritical, especially if a fresh sample spot is picked for every measurement. This was backed up experimentally by consecutive measurements (at the oxygen and fluorine K-edge) at the same sample spot, which did not reveal any apparent beam damage. For a detailed assessment of the SEI’s beam damage during XAS we refer to the SI under 2.3. *Dosage and Beam Damage Consideration* together with Figure S2 and Table S1.

Identification of the Solid Electrolyte Interphase Species

To identify possible SEI species we compare the SEI spectrum with the absorption spectra of several potential candidates. For this we have compiled a collection of oxygen K-edge reference spectra in Figure 7, where the SEI spectrum is shown as the white on grey background in each plot. We selected candidates based on two criteria: first, species with spectral contributions that could be correlated to the SEI spectrum and second, species commonly mentioned in literature as possible SEI components and we think are un-/likely be part of the SEI in our work. Our evaluation of how well a reference fingerprint matches the SEI spectrum is summarized in **Table 1**.

The SEI spectrum itself shows six distinct features to which the references are matched: (I) the rather asymmetric main peak at 533.0 eV with a broader shoulder at 531.4 eV (II) and a sharper shoulder at 533.5 eV (III); another pronounced peak at 535.6 eV (V); the main pre-edge valley (IV) at 534.5 eV; and one broad, single hump (VI) above the ionization edge at round 540 eV.

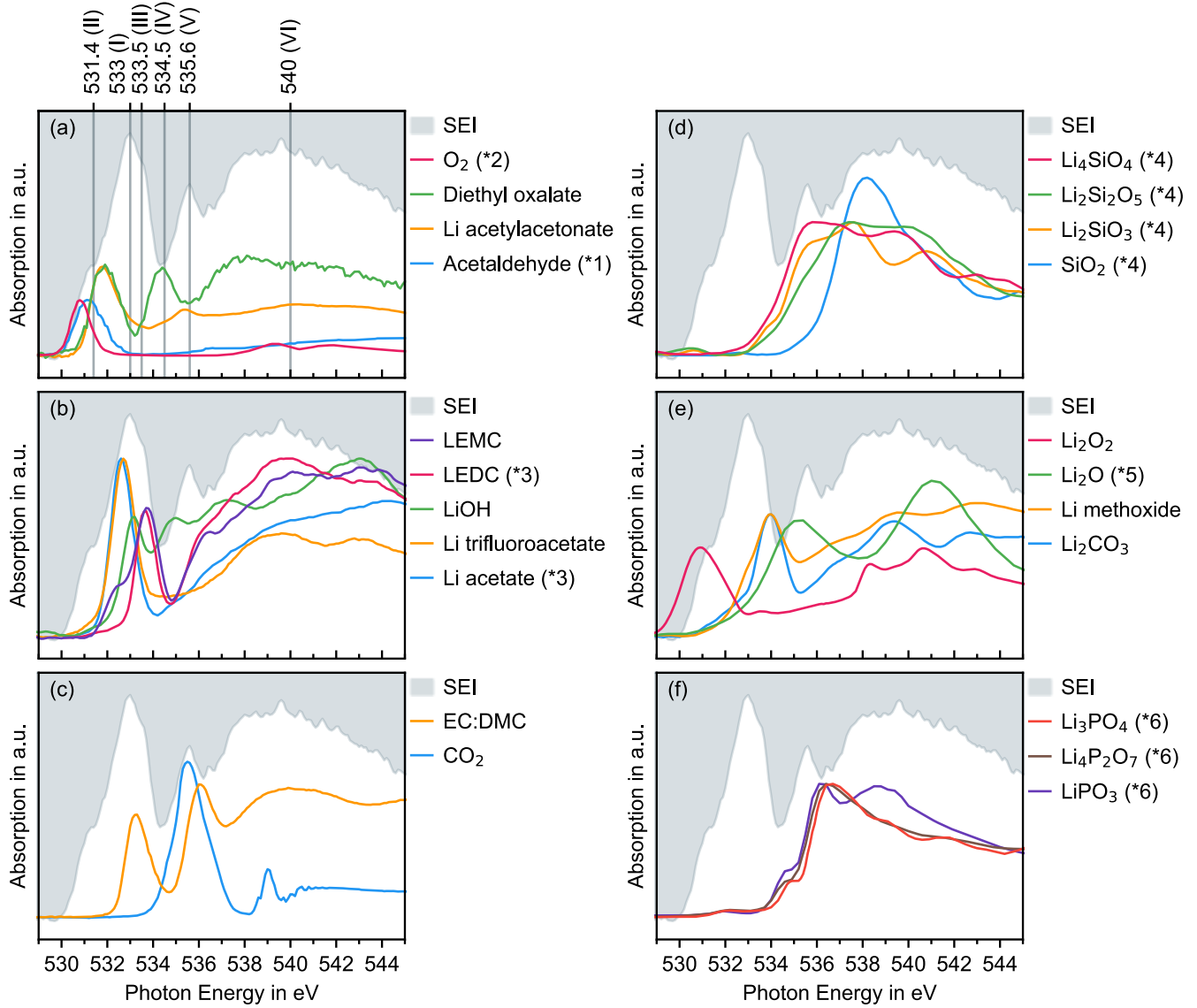


Figure 7: Comparison of the SEI spectrum (P6* from Figure 6d) to a variety of possible SEI reference species at the oxygen K-edge. The SEI spectrum is shown as the white on grey background throughout (a-f). The reference species are grouped by their possible correlation to the individual peaks (I) to (VI) as indicated in (a) or by the class of substance. **(a)** Pre-shoulder (II): O₂ (*2 from [75]), Diethyl oxalate, Li acetylacetonate and Acetaldehyde (*1 from [76]). **(b)** Main peak (I) and (III): LEMC, LEDC (*3), LiOH, Li trifluoroacetate, Li acetate (3* from [12]). **(c)** Second main peak (V): 1M LiPF₆ in EC:DMC and CO₂. **(d)** Lithium silicates: Li₄SiO₄, Li₂Si₂O₅, Li₂SiO₃, Li₂SiO₃ and SiO₂ (*4 from [77]). **(e)** Li₂O₂, Li₂O (*5 from [78], [79]), Li methoxide and Li₂CO₃. **(f)** Lithium phosphates: Li₃PO₄, Li₄P₂O₇ and LiPO₃ (*6 from [80]).

Table 1: Summary of the SEI species evaluation regarding their matching spectral fingerprint. L is likely, P is possible, and U is unlikely.

Name	Peak	Prob.	Name	Peak	Prob.	Name	Peak	Prob.
Li acetate	(I)	L	Li trifluoroacetate	(I)	L	LiOH	(I)	L
Acetaldehyde	(II)	L	Li acetylacetonate	(II)	L	LEDC	(III)	L
LEMC	(III)	L	CO ₂	(V)	L	EC:DMC	(V)	L
O ₂	(II)	P	Diethyl oxalate	(II)	P	SiO ₂	(VI)	P
Li ₂ SiO ₃	-	U	Li ₂ Si ₂ O ₅	-	U	Li ₄ SiO ₄	-	U
LiPO ₃	-	U	Li ₃ PO ₄	-	U	Li ₄ P ₂ O ₇	-	U
Li ₂ CO ₃	-	U	Li methoxide	-	U			
Li ₂ O	-	U	Li ₂ O ₂	-	U			

Based on the general trends of the carbonyl core $1s$ to π^* transition established by Urquhart *et al.* [64], we identified aldehyde functional groups as possible candidates that correspond to the broader pre-shoulder (II) at 531.4 eV. As one of the simplest molecules with an aldehyde group, acetaldehyde is shown in Figure 7a as a representative. The presence of liquid aldehyde species in the *Solid Electrolyte Interphase* may appear peculiar at first. However, a possible explanation may be given by the SEI model recently proposed by He *et al.* [81]. In their energy dispersive X-ray spectroscopy (EDX) tomography and cryogenic scanning TEM study on silicon nanowires, they observed a progressive growth of the SEI towards the center of the nanowire, leading to a strongly interwoven, “plum-pudding”-like morphology of silicon and SEI. This structural change is mediated by the proceeding formation and interconnection of pores, which form percolation channels for the electrolyte to permeate and be trapped in. Due to the X-ray micro spot ($85\ \mu\text{m} \times 25\ \mu\text{m}$), within the scope of our work presented here, we cannot spatially resolve the proposed “plum-pudding”-like morphology at the nanoscale. Nevertheless, the model of He *et al.* may give a first explanation for the presence of liquid aldehyde species within the SEI’s morphology. This would indicate, that the engulfed electrolyte may not only consist of the neat components EC:DMC, but also of aldehyde species as possible reduction products thereof.

It must be noted that O_2 gas has a sharp peak at 530.8 eV, too. Looking at the spectrum of the uncycled sample in Figure 6a, the bubble itself appears to have similar contribution, which could be correlated to a minor O_2 content inside the bubble. Consequently, the isolated SEI spectrum might still contain a contribution of the bubble O_2 , which was not fully accounted for by the subtraction of the uncycled sample. However, we thoroughly compared all cycled and uncycled XAS spectra in this region of interest (as shown in the SI with Figure S9) and are confident that the residual O_2 gas contribution in the isolated SEI spectrum, if present at all, is only minor. Thus, the pre-shoulder (II) at 531.4 eV mainly stems from acetaldehyde species as discussed earlier.

This is backed up by the slightly more fitting peak position of acetaldehyde over O₂ gas in Figure 7a.

Furthermore, in their work on the SEI on copper electrodes Zhuo *et al.* suggested the presence of oxalate species in their XAS data [12]. Based on this, we also identified diethyl oxalate (Figure 7a) as a possible contribution to (II). By screening several organic lithium compounds, we found that Li acetylacetonate like diethyl oxalate shows a peak at 531.6 eV but lacks the second peak at 534.3 eV. Considering that the second peak of diethyl oxalate directly coincides with the valley (IV) in the SEI spectrum, Li acetylacetonate seems a more likely match.

For the main peak (I) at 533.0 eV, we could not identify a species that contributes to this peak single-handedly. Besides, the asymmetric shape and the sharp shoulder (III) suggest that this peak is a convolution of peaks from several species. Based on the overall peak position, we identified lithium acetates, namely acetate and trifluoroacetate, and lithium hydroxide as possible involved species (see Figure 7b). While the overall spectral shapes of lithium acetate and lithium trifluoroacetate are in good agreement, the main peak is shifted by 0.1 eV from 532.6 eV to 532.7 eV for the acetate and trifluoroacetate, respectively. It is unclear if the shift is caused by the fluorination or stems from a discrepancy in energy calibration between our measurement and the values reported in the literature. However, besides the energy shift, the additional smaller peaks after the ionization edge for the trifluoroacetate indicate the former.

Lithium ethylene di-carbonate (LEDC) was commonly accepted as the main single-electron-pathway reduction product of EC and was assumed to be the main organic constituent of the SEI in EC-containing electrolytes [82]–[85]. However, there is still open debate if LEDC was mistaken for lithium ethylene mono-carbonate (LEMC) [14]. Our own measurement of LEMC and one of LEDC sourced from literature is shown in Figure 7b. It is very likely that either or both species contribute to the sharp side shoulder (III), but a distinction is hardly possible with the limited data. As with the acetates, the overall spectral shape of LEDC and LEMC is identical, but the main peak

is also shifted by 0.1 eV from 533.6 eV to 533.7 eV for LEDC and LEMC, respectively. We note that the spectral contribution at 532.5 eV in our own measurement of LEMC might be due to contamination of lithium acetate. Future measurements will determine if a discrimination between LEDC and LEMC based on their oxygen K-edge XAS spectra is experimentally possible. In any case, the spectral shape of LEMC, LEDC and the acetate species all fit the broader hump (VI) in the post-edge region of the SEI spectrum notably well.

We attribute the other pronounced peak (V) at 535.5 eV to the CO_2 1s to $2\pi_u$ transition and to the chain/ring π^* peak of EC:DMC, as shown in Figure 7c. Consequently, we assume the carbonyl π^* of EC:DMC contributes to (I) and (III) as well. This is in good agreement with our initial assumption that the electrolyte still contributes to the SEI spectrum.

For native oxide terminated silicon anodes it is reasonable to assume SiO_2 and lithium silicates ($\text{Li}_x\text{Si}_y\text{O}_z$) are part of the forming SEI. Based on *in-situ* synchrotron X-ray reflectivity and *ex-situ* X-ray photoelectron spectroscopy with first principles calculations, Cao *et al.* proposed a comprehensive picture of an inorganic SEI [86]. In their model, SiO_2 is transformed into an inorganic SEI layer made from Li_xSiO_y , Li_xSi and Li_2O , which in turn is covered by an organic SEI layer. Due to detection limitations and sample preparation constraints, they left the organic SEI layer somehow undefined. Cao *et al.* [86] specified the thickness of the inorganic SEI layer to be only 4 nm. Thus, the thin layer of lithium silicates may be overshadowed by the post-ionization edge spectral contribution of the organic layer and may be difficult to distinguish. Looking at Figure 7d, we consider the lithium silicates (Li_4SiO_4 , $\text{Li}_2\text{Si}_2\text{O}_5$, Li_2SiO_3) to be not apparent in the measured SEI spectrum, but we cannot fully rule out their presence in the SEI. Nevertheless, SiO_2 may still be present and contribute to the broader hump (VI) at around 538 eV.

Nevertheless, based on Figure 7e, we think the presence of Li_2O and Li_2O_2 is improbable. The missing pronounced peak can rule out the existence of Li_2O_2 at 531 eV and the distinct features past the ionization edge at 539 eV and 541 eV. For Li_2O , we would expect the second peak at

around 541 eV to be more present in the SEI spectrum's post ionization region and disturb the relatively smooth (VI) hump. As it was summarized by Heiskanen *et al.* [87], Li_2O is not a direct reduction product of the electrolyte but rather created over time upon the SEI's ageing. Thus, large quantities of Li_2O are not expected in the freshly prepared SEI investigated here.

The research on the SEI on graphite sparked many debates and one of the most debated examples is Li_2CO_3 as the main constituent of the SEI [3], [4]. While Li_2CO_3 was found in most studies, there is no common agreement whether it is indeed a SEI component or just an artefact through environmental exposure [8], [28], [88]. As it can be seen in Figure 7e, the main peak of Li_2CO_3 at 534.1 eV closely coincides with the main valley (IV), and thus it is unlikely that it contributes to the sharp side shoulder (III). While some small contribution of Li_2CO_3 could be overshadowed as a minor component in the pre-edge region, we would expect its distinctive features in the post-edge region at 539.2 eV and 542.8 eV to appear more apparent. In many XAS studies in literature, these post-edge features were the most evident and a distinct fingerprint of Li_2CO_3 while in many cases even overshadowing all other components [15], [16], [89], [90]. Based on this, we find the presence of Li_2CO_3 in the SEI on the silicon thin-film anodes investigated in this work to be unlikely, but we cannot rule out the presence in minor quantity. We note that Li methoxide has a strikingly similar spectral shape compared to Li_2CO_3 (see Figure 7e), whereby it could have easily been mistaken in literature before, especially in particularly noisy TEY and TFY XAS data.

Li *et al.* proposed that lithium phosphates $\text{Li}_x\text{P}_y\text{O}_z$ might be SEI constituents [90]. We show the absorption spectra of Li_3PO_4 , $\text{Li}_4\text{P}_2\text{O}_7$, and LiPO_3 in Figure 7f. The detection of the phosphates suffers from the identical drawbacks as the silicates, where organic species can easily overshadow their spectral contribution. While phosphates are not clearly present in our SEI spectra, we cannot rule out their presence in minor quantities either.

2.3.2. Fluorine K-Edge

We interpret the XAS data at the fluorine K-edge in analogy to the oxygen K-edge in Figure 6. Figure 8a shows the fluorine K-edge at three different sample positions, P1 to P3, from a cycled sample. The smaller the SH the more the spectral shape of the SEI is revealed. We can isolate the spectrum of the electrolyte by subtracting P3 from P1, which is shown in Figure 8b, and is in excellent agreement with the electrolyte spectrum of 1M LiPF₆ in EC:DMC. At the fluorine K-edge the electrolyte spectrum correlates to the 1M LiPF₆ salt dissolved in EC:DMC and a reference TEY XAS spectrum of LiPF₆ powder are given in Figure 8b accordingly.

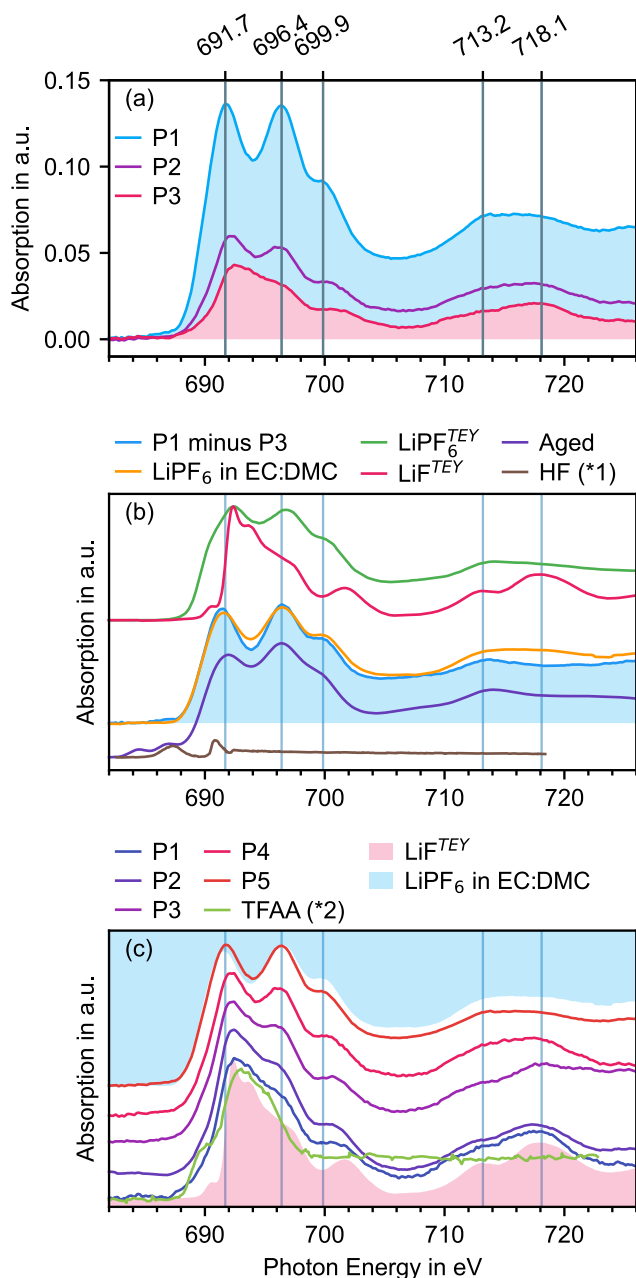


Figure 8: Isolation and identification of the SEI species at the fluorine K-edge. **(a)** Fluorine K-edge transmission sXAS spectra of a cycled sample at 3 different sample positions P1 to P3. Contribution of the electrolyte salt LiPF₆ is shaded in blue and the contribution of the SEI is shaded in red. **(b)** Extraction of the electrolyte salt LiPF₆ spectrum that sits on top of the SEI by subtracting P3 from P1. Reference spectra of 1M LiPF₆ in EC:DMC, LiPF₆ powder (TEY) and LiF powder (TEY) are shown for comparison. Additionally, fluorine K-edge transmission sXAS spectrum of an aged cell (mean value of 4 spectra) together with a reference spectrum of HF (*1 from [91]). Spectra are stacked vertically by an arbitrary value. **(c)** Fluorine K-edge transmission sXAS spectra of cycled samples at 5 different positions P1 to P5. The spectra are normalized to the individual highest absorption value and stacked vertically by an arbitrary value. Reference measurements of 1M LiPF₆ in EC:DMC, LiF powder (TEY) and trifluoroacetic acid (TFAA) are shown for comparison (*2 from [92]).

In Figure 8a, P1 shows two main peaks at 691.7 eV (I) and 696.4 eV (II) photon energy with a peak ratio of 1.02, and a side peak at 699.9 eV (III), as well as a broader peak between 713.2 and 718.1 eV. From P1 to P3, the first main peak (I) shifts slightly to higher energies and the spectral

contribution of the second main peak (II) decreases while the side peak (III) shifts to higher energies as well. Figure 8c shows the fluorine K-edge of cycled samples at 5 different positions with the main peak (I) normalized to one to emphasize the changes. P1 to P5 have increasing pre-normalization SH values, where P1 reveals the SEI the most. We identify LiF as the main SEI species by comparing the overall spectral shapes at the fluorine K-edge. A TEY XAS reference spectrum of LiF powder is given in Figure 8b and Figure 8c for comparison. Additionally, P1 to P3 in Figure 8b shows an additional side shoulder at slightly higher energies than the main LiF peak. We propose that this peak could hint at trifluoroacetic acid (TFAA) species in the SEI, as shown by the reference spectrum in Figure 8c. We suggest that this may be correlated to the Li acetate species we presumably identified at the oxygen K-edge (compare Figure 7). The lithium acetate may be fluorinated and therefore shows up as TFAA species at the fluorine K-edge.

The isolated electrolyte spectrum (P1 minus P3) and the reference 1M LiPF₆ in EC:DMC electrolyte spectrum in Figure 8b both show a peak ratio of 0.97 between the main peaks (I) and (II). Hence, we consider any discrepancy in this ratio as an indication for underlying SEI species. This can be seen for P1 where its peak ratio of 1.02 can be correlated to the underlying spectral contribution of the LiF. Due to synchrotron time constraints, we were unable to obtain fluorine K-edge spectra from uncycled samples to check and compare for any spectral fingerprints of beam damage. However, because both the isolated electrolyte spectrum, P1 minus P3, and 1M LiPF₆ in EC:DMC show a peak ratio of 0.97, we assume the beam damage caused by the bubble formation is minimal, and the LiF indeed correlates to the SEI formed through the electrochemical cycling. We consider our LiPF₆ TEY reference measurement shown in Figure 8b to be contaminated with LiF as well, due to its I-to-II peak ratio of 1.02. We still include it to show the overall spectral fingerprint of LiPF₆.

Similarly, the aged sample in Figure 8b exhibits an I-to-II peak ratio of 0.95, again hinting at fluorine species that develop as ageing products without any electrochemical procedure. This also comes

apparent from the additional pronounced peaks at 684.46 eV and 686.87 eV. We correlate the second peak at 686.87 eV to the presence of hydrogen fluoride (HF) (compare the reference spectrum in Figure 8b). The evolution of HF is a known phenomenon in lithium-ion battery technology and is often connected to water and moisture contamination of the electrolyte or cell. We take the absence of any HF signal in non-aged samples as confirmation that water and moisture contamination is not an issue for the 12-hour time frame of our *in-situ* measurements. On top of that, outlier samples which hint at the presence of further SEI species at the fluorine K-edge but could not be observed throughout all samples are discussed in the SI under *10. Fluorine K-edge Outliers* and Figure S10.

2.3.3. Silicon L-edge

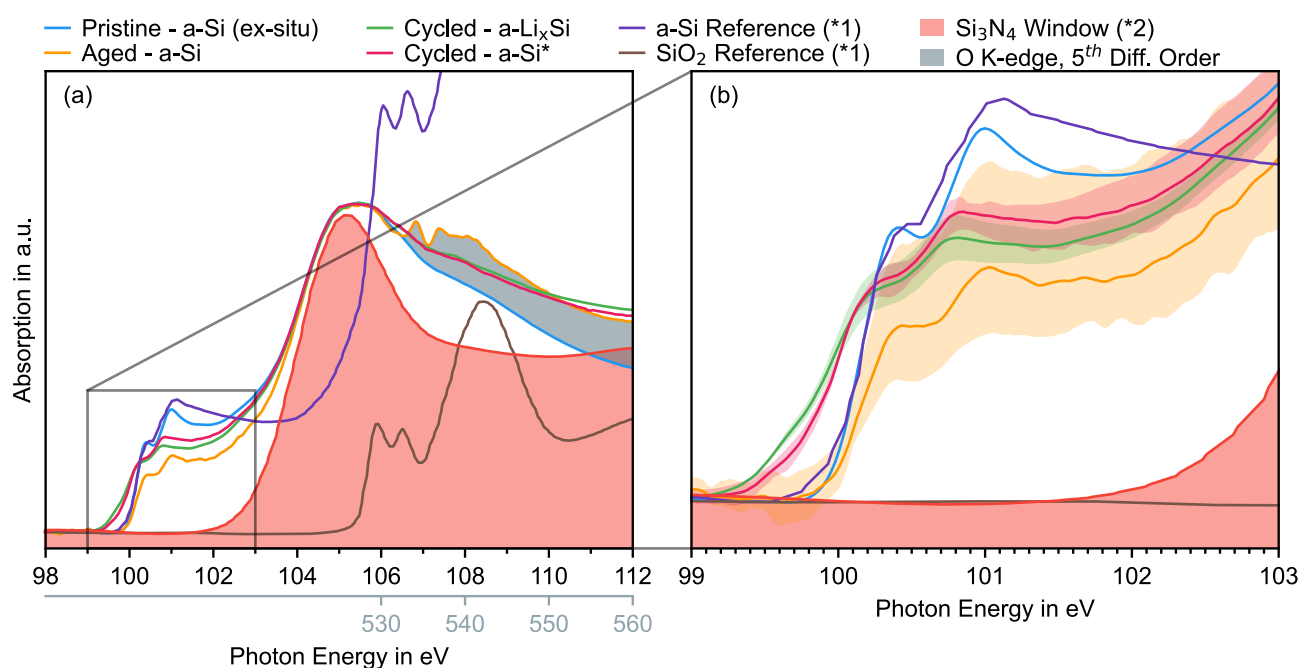


Figure 9: Silicon L-edge transmission sXAS spectra of a pristine silicon thin-film anode under *ex-situ* conditions, aged and cycled samples in the energy range from 98 eV to 112 eV. The boundaries of the filled areas (b) are the minimum and maximum values and the solid line is the mean value from several individual spectra for the pristine sample, aged, cycled - Li_xSi and cycled - a-Si*, respectively. Reference spectra of amorphous silicon (a-Si), SiO₂, and Si₃N₄ are shown alongside for comparison (*1 from [93], *2 from [94]). Due to the nature of undulator radiation and the plane grating monochromator of the U49-2_PGM-1 [70] beamline, the radiation in the energy region of the silicon L-edge also contains contributions of higher energy photons. The monochromator setting for the silicon L-edge energy range coincides with the fifth diffraction order for higher energetic photons from the oxygen K-edge between 490 eV and 560 eV. The photon energy scale is given accordingly. The respective absorption that stems from the supposedly overlap of the silicon L-edge and the oxygen K-edge is marked in grey.

The de-/lithiation of the silicon thin-film anodes can be observed at the silicon L-edge. Figure 9 shows silicon *in-situ* L-edge XAS spectra of the aged and cycled anodes together with a pristine sample obtained from an empty cell without electrolyte, i.e., under *ex-situ* conditions. The overall spectral shape of the samples at the silicon L-edge is dominated by the broad absorption hump from the SiN_x windows at around 105 eV photon energy. A reference spectrum from silicon nitride Si₃N₄ is shown in Figure 9, too. Silicon exhibits additional spectral features between 99 eV and 102 eV. In this energy region, the spectrum of the pristine amorphous silicon thin-film anode resembles a reference spectrum of amorphous silicon (a-Si) from the literature [93]. However, the two main peaks of a-Si at 100.4 eV and 101.0 eV appear to be much better resolved in our transmission setup compared to the usual TEY measurements common in literature. We explain this with the surface sensitivity of the TEY measurement that picks up the interfering signal of the native SiO₂ layer; see for comparison the SiO₂ reference spectrum in Figure 9a.

Consequently, the overall spectral shape of the samples can be interpreted as a linear combination of the 50 nm thick sample itself with two SiN_x windows, 50 nm in thickness each. The aged sample shows the same spectral shape as the pristine *ex-situ* sample, demonstrating that the *ex-situ* measurement can be reproduced with our *in-situ* bubble approach and shows that the silicon thin-film itself does not undergo any ageing process, e.g., oxidation to SiO₂. We assume here for the aged sample that the bubble formation did not sufficiently remove the excess electrolyte. The resulting thicker electrolyte layer shows up as an artificial erroneous absorption signal in the energy range from 106 eV to 112 eV and correlates to the oxygen K-edge in the fifth diffraction order from 530 eV to 560 eV. The corresponding energy scale of the fifth diffraction order is given in Figure 9a accordingly.

We notice from the cycled samples that the lithiation broadens the two main peaks of the a-Si (100.4 eV and 101.0 eV), slightly shifts them to lower energies, and that a broad side shoulder at around 99.6 eV emerges. We further assume the bubble formation freezes the degree of lithiation

in time, because the bubble formation pushes away most electrolyte. The bubble was created at 0.53 V during the delithiation sweep and at 0.44 V during the lithiation sweep for the two samples shown in Figure 9. Based on section 2.2, we correlate the different spectral shapes to a-Si* and a-Li_xSi, respectively. Thus, we attribute the differences to an increased degree of lithiation. We will establish a more fine-grained correlation with future experiments. Ultimately, we aim to correlate the degree of lithiation to the SEI composition.

Overall, the spectral shape of the *in-situ* samples at the Silicon L-edge can entirely be explained by the lithiation of a-Si and the underlying spectral contribution of the SiN_x windows. No additional peaks of further silicon-containing SEI species can be observed. Thus, although lithium silicates and phosphates were proposed in the literature, we could not verify their presence in the SEI at the silicon L-edge.

3. Conclusion

In summary, we introduced a novel approach for transmission XAS on liquids and thin-film battery electrode materials in the soft X-ray regime under *in-situ* conditions. Our unique method puts a novel twist to conventional SiN_x window-based liquid cells by utilizing a deliberately induced gas-bubble to form a soft X-ray transparent thin electrolyte layer. With our new approach we investigated the SEI composition on silicon thin-film anodes, which were cycled ten times between 10 mV and 800 mV vs. Li/Li⁺.

As summarized in Table 1, based on spectral sXAS fingerprints at the oxygen K-edge, we identified acetates (based on Li acetate and Li trifluoroacetate), Li ethylene carbonates (based on LEMC and LEDC), acetonates (based on Li acetylacetonate), and LiOH as the solid species which are most likely to be present in the SEI on the silicon anodes investigated in this work. At the fluorine K-edge we identified LiF to be the main fluorine-containing species in the SEI. Besides this, we suspect that the acetate species may be fluorinated and hence can be correlated to the

observed trifluoroacetic acid fingerprint. Furthermore, even though reported in the literature, from our oxygen K-edge and silicon L-edge spectra we could not find clear evidence of lithium silicates or lithium phosphates.

LEMC or LEDC (the ongoing dispute aside [14]) are accepted to be the main reduction products of EC-containing electrolytes and together with LiF were found in many SEIs on both graphite and silicon [4], [8], [14], [60], [85], [87], [90], [95]–[98]. Thus, our results clearly demonstrate the feasibility of our novel approach to investigate the SEI on silicon anodes through transmission sXAS. However, we found acetate species to be more likely to make up the biggest SEI contribution over LEMC or LEDC. As Schroder *et al.* demonstrated for crystalline silicon anodes, the electrochemical preparation heavily influences the SEI's composition [28]. Based on this, with the current data, it is too early to evaluate whether the increased acetate content is of general nature and was revealed through our *in-situ* measurements or is specific to our approach with the chosen electrochemical treatment. With future measurements we plan to establish a connection between the electrochemical preparation and the SEI's composition.

We still want to mention that we also found evidence for the presence of liquid aldehyde species at the oxygen K-edge. While liquid species in the *Solid Electrolyte Interphase* admittedly sound peculiar at first, a possible early explanation for their presence may be given by the SEI model recently proposed by He *et al.* [81]. Based on their TEM and EDX tomography work on silicon nanowires, He *et al.* describe the silicon and its SEI as a “plum-pudding”-like structure in which's interconnected pores the liquid electrolyte can permeate and be trapped in. Based on the similar dimensions (60-90 nm wire diameter vs. 50 nm film thickness) we think their model is applicable to our work. Here, our complementary spectroscopic findings could indicate, that the entrapped electrolyte (localized through the EDX mapping of oxygen) may not only consist of the neat components EC:DMC, but also of aldehyde species as possible reduction products thereof.

However, due to the limited resolution given by the X-ray micro spot size, the “plum-pudding”-like morphology at the nanoscale could not be spatially resolved in this work and further investigation is needed. For this we imagine the future adaption of our cell/approach to scanning transmission X-ray microscopes at the BESSY II facility, which would allow nanoscale resolution.

4. Experimental

Electrochemistry

The silicon thin-film anodes were cycled via linear sweep voltammetry (LSV) using a potentiostat (Interface 1010T, Gamry Instruments) inside our electrochemical cell. All potentials are given vs. Li/Li⁺. Sweeps with decreasing potential are referred to as lithiation sweeps while sweeps with increasing potential as delithiation sweeps. The scan speed in all sweeps was 0.5 mV s⁻¹. The initial lithiation sweep ran from the individual OCP value (usually around 3.2 V for Si vs. Li) down to 10 mV. Afterward, the anodes were cycled for a given number of times between 10 mV to 800 mV. Between every lithiation and delithiation sweep the anodes were potentiostatically held at 10 mV for a certain amount of time depending on our experimental goal.

Sample Catalogue

For the *in-situ* XAS investigation in this work, we present samples, that differ in their electrochemical treatment or the lack thereof. The different treatments were chosen to understand our measurement approach better and distinguish between the SEI formed by the electrochemistry itself and all possible by-products through the bubble formation/beam damage and ageing processes, together with all possible contaminations. We use the terms sample and cell interchangeably. All cells were prepared conventionally, as described in 2.1. *Cell Design*. The samples discussed in this work are summarized in Table 2, together with the corresponding electrochemical treatment, the cell configuration, the sample size, and the measurement time. The sample size refers to the number of cells from which each label's data was compiled. A statistical

assessment of the aged, uncycled and cycled cells regarding the spectral shape in the pre-peak region of the oxygen K-edge, particularly important for the identification of the SEI, is given in the SI under 9. *In-situ* SEI Overview and Figure S9.

Table 2: Catalogue of *in-situ* samples/cells with corresponding electrochemical treatment, electrode cell configuration, sample size and the delay between measurement and cell assembly.

Label	El. chem. treatment	Cell configuration	Sample size	Delay
Aged	No	With electrodes	1	4 days under atm. cond.
Uncycled	No	With electrodes	1	No delay
Cycled	10 cycles, 1 ks potentiostatic holding time at 10 mV	With electrodes	3	No delay
1M LiPF ₆ in DMC	No	No electrodes	1	No delay
1M LiPF ₆ in EC:DMC	No	No electrodes	4	No delay

X-ray Absorption Spectroscopy

The sXAS was performed at the U49-2_PGM-1 [70] and UE56-2_PGM-2 beamlines of the BESSY II synchrotron facility in Berlin using the SOL³PES [99] and LiXEdrom [100] experimental stations. Both stations were operated under high vacuum conditions of 2×10^{-6} mbar.

The transmission signal was measured with a GaAsP (Hamamatsu G1127) or GaP (ifw optronics JEP5-365) photodiode and an electrometer (Keithley 6514). For the *in-situ* measurements at the U49-2_PGM-1 beamline, the slit size was set to 5 μm , which correlates to a focal size of about 85 μm x 25 μm [70] at the sample position. Hence, the focal size was sufficiently small to probe the sample at several different positions within the 500 μm x 500 μm SiN_x windows. This allowed us to pick a fresh sample spot for each measurement and avoided noticeable beam damage effects. To decrease the data acquisition time and minimize the radiation dose, the absorption spectra were recorded in continuous mode - monochromator and undulator were accelerated once and then move synchronously through the desired spectral region [101]. For representative measurements, we estimated a total dose below 2 μJ at the oxygen K-edge and about 5 μJ at the fluorine K-edge for each recorded spectrum, respectively. This estimation is described in more

detail in the SI under 2.3. *Dosage and Beam Damage Consideration* based on Figure S1 and Figure S2.

The absorption was calculated from blank measurements of the bare photodiode each day. Both the blank and the sample measurement themselves were normalized by the individual drain current of the refocusing mirror upstream, which was again measured with an electrometer (Keithley 6514). The diode and mirror current were measured simultaneously, by triggering the electrometers synchronously through their GPIB interface. The background of the absorption spectra was removed by fitting linear slopes to the pre- and post- ionization edge regions. Because the exact ionization edge-step function is unknown, the transition between both slopes was approximated by a second-degree Bezier curve. The energy in the oxygen K-edge region was calibrated to the 1s to $2\pi_u$ transition of CO₂ at 535.5 eV photon energy from a reference gas transmission spectrum measurement at the end of each day. Alternatively, the energy values were calibrated by aligning the blank diode current signals. At the fluorine K-edge we relied on the energy calibration of the U49-2_PGM-1 [70] beamline. The full data treatment, i.e., the calculation of the absorption signal, the energy calibration, and the background subtraction procedure, is described in more detail in the SI under 5. *Data Treatment*. Furthermore, reference compounds commercially available as powders were ground in a mortar and deposited onto a conductive carbon tape or pressed into an indium foil. The measured reference powders and liquids were: 1M LiPF₆ in EC:DMC (Battery Grade, Sigma-Aldrich), 1M LiPF₆ in DMC (Battery Grade, Sigma-Aldrich), Diethyl oxalate (98%, TCI Europe), Li acetylacetonate (98%, Sigma-Aldrich), Lithium ethylene mono-carbonate (LEMC) (GenoSynth GmbH), LiOH (anhydrous 98%, Alfa Aesar), Li trifluoroacetate (97% Alfa Aesar), Li₂O₂ (95%, Acros Organics), Li methoxide (98%, Sigma-Aldrich), Li₂CO₃ (99%, Sigma-Aldrich), LiF (99.98 trace metal basis, Sigma-Aldrich), LiPF₆ (98%, Alfa Aesar). The preparation was done in an argon glovebox (M. BRAUN, O₂ and H₂O kept <0.1 ppm) and the samples were brought to the experimental station in a sealed container. For

the transfer into the vacuum chamber the time of air exposure was kept under 30 sec. For LEMC as a particular air-sensitive sample, an Argon-filled glove bag (AtmosBag, Sigma-Aldrich) was used for the transfer and the experimental chamber was flushed with Argon priorly. The absorption spectra of the powder references were obtained through the Total Electron Yield (TEY) signal, measured as the drain current by an electrometer (Keithley 6514). Absorption spectra of reference compounds that are commercially available as liquids were recorded in transmission with our cell. The cell was assembled with two uncoated SiN_x membrane windows inside a glove bag (AtmosBag, Sigma-Aldrich) that was flushed with Argon.

UV/Vis-Spectroscopy and Optical Microscopy

To monitor the de-/lithiation of the silicon thin-film anodes we performed *operando* (UV/Vis) and optical microscopy during the cycling procedure. We coupled a “Flame UV-VIS Spectrometer” (200-850 nm) from Ocean Insight into the cell using uncollimated standard step-index multimode fiber optic patch cables (Thorlabs, Inc.). A mercury-xenon short-arc benchtop lamp (Thorlabs, Inc.) was used as a light source. Because the absorption changes upon de-/lithiation, we modified the spectrometer software to dynamically adjust the spectrometer's integration time to keep the xenon line at 828 nm at a fixed exposure value. A “Researcher Trino 40-1000x” from Bresser GmbH was used for the optical microscopy.

Supporting Information

Supporting Information is available from the Wiley Online Library or from the author.

Acknowledgements

Access to the COMSOL Multiphysics® software package was supported by the Helmholtz Energy Materials Foundry (HEMF), a large-scale distributed research infrastructure founded by the German Helmholtz Association.

The authors thank the Energy Materials In-Situ Laboratory Berlin (EMIL) for access to the sample preparation and characterization environment.

The authors thank Dr. Engin Özkol from TU Delft for the preparation of the silicon thin-films at the Energy Materials In-Situ Laboratory Berlin (EMIL).

The authors thank Karsten Harbauer from the Institute Solar Fuels at HZB for the metallization of the sample substrates.

WQG and RS acknowledge funding from the Deutsche Forschungsgemeinschaft (DFG, German Research Foundation) through an Emmy-Noether grant (SE 2253/3-1). All authors thank the HZB staff for support during the beamtimes at BESSY II.

References

- [1] K. Feng *et al.*, “Silicon-Based Anodes for Lithium-Ion Batteries: From Fundamentals to Practical Applications,” *Small*, vol. 14, no. 8, p. 1702737, Feb. 2018, doi: 10.1002/smll.201702737.
- [2] M. Li, J. Lu, Z. Chen, and K. Amine, “30 Years of Lithium-Ion Batteries,” *Adv. Mater.*, vol. 30, no. 33, p. 1800561, Aug. 2018, doi: 10.1002/adma.201800561.
- [3] K. Xu, “Electrolytes and Interphases in Li-Ion Batteries and Beyond,” *Chem. Rev.*, vol. 114, no. 23, pp. 11503–11618, Dec. 2014, doi: 10.1021/cr500003w.
- [4] P. Verma, P. Maire, and P. Novák, “A review of the features and analyses of the solid electrolyte interphase in Li-ion batteries,” *Electrochim. Acta*, vol. 55, no. 22, pp. 6332–6341, Sep. 2010, doi: 10.1016/j.electacta.2010.05.072.
- [5] C. K. Chan, R. Ruffo, S. S. Hong, and Y. Cui, “Surface chemistry and morphology of the solid electrolyte interphase on silicon nanowire lithium-ion battery anodes,” *J. Power Sources*, vol. 189, no. 2, pp. 1132–1140, Apr. 2009, doi: 10.1016/j.jpowsour.2009.01.007.
- [6] M. Winter, “The solid electrolyte interphase - The most important and the least understood solid electrolyte in rechargeable Li batteries,” *Zeitschrift für Phys. Chemie*, vol. 223, no. 10–11, pp. 1395–1406, 2009, doi: 10.1524/zpch.2009.6086.
- [7] M. Nie, D. Chalasani, D. P. Abraham, Y. Chen, A. Bose, and B. L. Lucht, “Lithium ion battery graphite solid electrolyte interphase revealed by microscopy and spectroscopy,” *J. Phys.*

- Chem. C*, vol. 117, no. 3, pp. 1257–1267, 2013, doi: 10.1021/jp3118055.
- [8] K. Edström, M. Herstedt, and D. P. Abraham, “A new look at the solid electrolyte interphase on graphite anodes in Li-ion batteries,” *J. Power Sources*, vol. 153, no. 2, pp. 380–384, 2006, doi: 10.1016/j.jpowsour.2005.05.062.
- [9] T. Yoshida *et al.*, “Degradation Mechanism and Life Prediction of Lithium-Ion Batteries,” *J. Electrochem. Soc.*, vol. 153, no. 3, p. A576, 2006, doi: 10.1149/1.2162467.
- [10] S. Malmgren *et al.*, “Comparing anode and cathode electrode/electrolyte interface composition and morphology using soft and hard X-ray photoelectron spectroscopy,” *Electrochim. Acta*, vol. 97, pp. 23–32, 2013, doi: 10.1016/j.electacta.2013.03.010.
- [11] P. Lu, C. Li, E. W. Schneider, and S. J. Harris, “Chemistry, impedance, and morphology evolution in solid electrolyte interphase films during formation in lithium ion batteries,” *J. Phys. Chem. C*, vol. 118, no. 2, pp. 896–903, 2014, doi: 10.1021/jp4111019.
- [12] Z. Zhuo *et al.*, “Breathing and oscillating growth of solid-electrolyte-interphase upon electrochemical cycling,” *Chem. Commun.*, vol. 54, no. 7, pp. 814–817, 2018, doi: 10.1039/C7CC07082A.
- [13] S. Shi *et al.*, “Direct calculation of Li-ion transport in the solid electrolyte interphase,” *J. Am. Chem. Soc.*, vol. 134, no. 37, pp. 15476–15487, 2012, doi: 10.1021/ja305366r.
- [14] L. Wang *et al.*, “Identifying the components of the solid–electrolyte interphase in Li-ion batteries,” *Nat. Chem.*, vol. 11, no. 9, pp. 789–796, Sep. 2019, doi: 10.1038/s41557-019-0304-z.
- [15] S. J. Rezvani *et al.*, “SEI Dynamics in Metal Oxide Conversion Electrodes of Li-Ion Batteries,” *J. Phys. Chem. C*, vol. 121, no. 47, pp. 26379–26388, Nov. 2017, doi: 10.1021/acs.jpcc.7b08259.

- [16] S. J. Rezvani *et al.*, “Is the Solid Electrolyte Interphase an Extra-Charge Reservoir in Li-Ion Batteries?,” *ACS Appl. Mater. Interfaces*, vol. 9, no. 5, pp. 4570–4576, 2017, doi: 10.1021/acsami.6b12408.
- [17] J. W. Smith and R. J. Saykally, “Soft X-ray Absorption Spectroscopy of Liquids and Solutions,” *Chem. Rev.*, vol. 117, no. 23, pp. 13909–13934, 2017, doi: 10.1021/acs.chemrev.7b00213.
- [18] M. Nagasaka, H. Yuzawa, and N. Kosugi, “Development and application of in situ/operando soft X-ray transmission cells to aqueous solutions and catalytic and electrochemical reactions,” *J. Electron Spectros. Relat. Phenomena*, vol. 200, pp. 293–310, 2015, doi: 10.1016/j.elspec.2015.05.012.
- [19] N. Huse *et al.*, “Probing the hydrogen-bond network of water via time-resolved soft X-ray spectroscopy,” *Phys. Chem. Chem. Phys.*, vol. 11, no. 20, pp. 3951–3957, 2009, doi: 10.1039/b822210j.
- [20] S. Schreck, G. Gavrilu, C. Weniger, and P. Wernet, “A sample holder for soft x-ray absorption spectroscopy of liquids in transmission mode,” *Rev. Sci. Instrum.*, vol. 82, no. 10, p. 103101, Oct. 2011, doi: 10.1063/1.3644192.
- [21] K. K. Goncz, P. Batson, D. Ciarlo, B. W. Loo, and S. S. Rothman, “An environmental sample chamber for X-ray microscopy,” *J. Microsc.*, vol. 168, no. 1, pp. 101–110, 1992, doi: 10.1111/j.1365-2818.1992.tb03254.x.
- [22] J. R. Dwyer and M. Harb, “Through a Window, Brightly: A Review of Selected Nanofabricated Thin-Film Platforms for Spectroscopy, Imaging, and Detection,” *Appl. Spectrosc.*, vol. 71, no. 9, pp. 2051–2075, Sep. 2017, doi: 10.1177/0003702817715496.
- [23] J. M. Grogan, N. M. Schneider, F. M. Ross, and H. H. Bau, “Bubble and Pattern Formation in Liquid Induced by an Electron Beam,” *Nano Lett.*, vol. 14, no. 1, pp. 359–364, Jan. 2014,

doi: 10.1021/nl404169a.

- [24] COMSOL AB, "COMSOL Multiphysics®." Stockholm, Sweden, 2018, [Online]. Available: www.comsol.com.
- [25] R. Jafari and T. Okutucu-Özyurt, "Phase-Field Modeling of Vapor Bubble Growth in a Microchannel," *J. Comput. Multiph. Flows*, vol. 7, no. 3, pp. 143–158, Sep. 2015, doi: 10.1260/1757-482X.7.3.143.
- [26] M. Kawaji and P. M. Y. Chung, "Adiabatic gas-liquid flow in microchannels," *Microscale Thermophys. Eng.*, vol. 8, no. 3, pp. 239–257, 2004, doi: 10.1080/10893950490477518.
- [27] H. Xia, S. Tang, and L. Lu, "Properties of amorphous Si thin film anodes prepared by pulsed laser deposition," *Mater. Res. Bull.*, vol. 42, no. 7, pp. 1301–1309, Jul. 2007, doi: 10.1016/j.materresbull.2006.10.007.
- [28] K. W. Schroder, H. Celio, L. J. Webb, and K. J. Stevenson, "Examining Solid Electrolyte Interphase Formation on Crystalline Silicon Electrodes: Influence of Electrochemical Preparation and Ambient Exposure Conditions," *J. Phys. Chem. C*, vol. 116, no. 37, pp. 19737–19747, Sep. 2012, doi: 10.1021/jp307372m.
- [29] K. W. Schroder, A. G. Dylla, S. J. Harris, L. J. Webb, and K. J. Stevenson, "Role of surface oxides in the formation of solid-electrolyte interphases at silicon electrodes for lithium-ion batteries," *ACS Appl. Mater. Interfaces*, vol. 6, no. 23, pp. 21510–21524, 2014, doi: 10.1021/am506517j.
- [30] Y. Y. Tang *et al.*, "Cobalt nanomountain array supported silicon film anode for high-performance lithium ion batteries," *Electrochim. Acta*, vol. 88, pp. 664–670, Jan. 2013, doi: 10.1016/j.electacta.2012.10.119.
- [31] A. Reyes Jiménez *et al.*, "A Step toward High-Energy Silicon-Based Thin Film Lithium Ion

- Batteries,” *ACS Nano*, vol. 11, no. 5, pp. 4731–4744, May 2017, doi: 10.1021/acsnano.7b00922.
- [32] T. L. Kulova, A. M. Skundin, Y. V. Pleskov, E. I. Terukov, and O. I. Kon’kov, “Lithium insertion into amorphous silicon thin-film electrodes,” *J. Electroanal. Chem.*, vol. 600, no. 1, pp. 217–225, 2007, doi: 10.1016/j.jelechem.2006.07.002.
- [33] T. Ikonen, T. Nissinen, E. Pohjalainen, O. Sorsa, T. Kallio, and V. P. Lehto, “Electrochemically anodized porous silicon: Towards simple and affordable anode material for Li-ion batteries,” *Sci. Rep.*, vol. 7, no. 1, pp. 1–8, 2017, doi: 10.1038/s41598-017-08285-3.
- [34] S. Bourderau, T. Brousse, and D. M. Schleich, “Amorphous silicon as a possible anode material for Li-ion batteries,” *J. Power Sources*, vol. 81–82, pp. 233–236, 1999, doi: 10.1016/S0378-7753(99)00194-9.
- [35] A. Ronneburg *et al.*, “Morphological evolution of a single crystal silicon battery electrode during lithiation and delithiation: An operando phase-contrast imaging study,” *Energy Storage Mater.*, vol. 32, no. July, pp. 377–385, 2020, doi: 10.1016/j.ensm.2020.06.007.
- [36] W. . Weydanz, M. Wohlfahrt-Mehrens, and R. . Huggins, “A room temperature study of the binary lithium–silicon and the ternary lithium–chromium–silicon system for use in rechargeable lithium batteries,” *J. Power Sources*, vol. 81–82, pp. 237–242, Sep. 1999, doi: 10.1016/S0378-7753(99)00139-1.
- [37] C. J. Wen and R. A. Huggins, “Chemical diffusion in intermediate phases in the lithium-silicon system,” *J. Solid State Chem.*, vol. 37, no. 3, pp. 271–278, May 1981, doi: 10.1016/0022-4596(81)90487-4.
- [38] H. Okamoto, “The Li-Si (Lithium-Silicon) system,” *Bull. Alloy Phase Diagrams*, vol. 11, no. 3, pp. 306–312, Jun. 1990, doi: 10.1007/BF03029305.

- [39] M. T. McDowell, S. W. Lee, W. D. Nix, and Y. Cui, "25th Anniversary Article: Understanding the Lithiation of Silicon and Other Alloying Anodes for Lithium-Ion Batteries," *Adv. Mater.*, vol. 25, no. 36, pp. 4966–4985, Sep. 2013, doi: 10.1002/adma.201301795.
- [40] P. Limthongkul, Y.-I. Jang, N. J. Dudney, and Y.-M. Chiang, "Electrochemically-driven solid-state amorphization in lithium-silicon alloys and implications for lithium storage," *Acta Mater.*, vol. 51, no. 4, pp. 1103–1113, Feb. 2003, doi: 10.1016/S1359-6454(02)00514-1.
- [41] M. Kim, Z. Yang, and I. Bloom, "Review—The Lithiation/Delithiation Behavior of Si-Based Electrodes: A Connection between Electrochemistry and Mechanics," *J. Electrochem. Soc.*, vol. 168, no. 1, p. 010523, Jan. 2021, doi: 10.1149/1945-7111/abd56f.
- [42] M. N. Obrovac and V. L. Chevrier, "Alloy Negative Electrodes for Li-Ion Batteries," *Chem. Rev.*, vol. 114, no. 23, pp. 11444–11502, Dec. 2014, doi: 10.1021/cr500207g.
- [43] C.-M. Wang *et al.*, "In Situ TEM Investigation of Congruent Phase Transition and Structural Evolution of Nanostructured Silicon/Carbon Anode for Lithium Ion Batteries," *Nano Lett.*, vol. 12, no. 3, pp. 1624–1632, Mar. 2012, doi: 10.1021/nl204559u.
- [44] T. D. Hatchard and J. R. Dahn, "In Situ XRD and Electrochemical Study of the Reaction of Lithium with Amorphous Silicon," *J. Electrochem. Soc.*, vol. 151, no. 6, p. A838, 2004, doi: 10.1149/1.1739217.
- [45] V. L. Chevrier and J. R. Dahn, "First Principles Studies of Disordered Lithiated Silicon," *J. Electrochem. Soc.*, vol. 157, no. 4, p. A392, 2010, doi: 10.1149/1.3294772.
- [46] J. Li, A. Smith, R. J. Sanderson, T. D. Hatchard, R. A. Dunlap, and J. R. Dahn, "In Situ [sup 119]Sn Mössbauer Effect Study of the Reaction of Lithium with Si Using a Sn Probe," *J. Electrochem. Soc.*, vol. 156, no. 4, p. A283, 2009, doi: 10.1149/1.3073879.
- [47] M. N. Obrovac and L. J. Krause, "Reversible Cycling of Crystalline Silicon Powder," *J.*

Electrochem. Soc., vol. 154, no. 2, p. A103, 2007, doi: 10.1149/1.2402112.

- [48] J. W. Wang *et al.*, “Two-Phase Electrochemical Lithiation in Amorphous Silicon,” *Nano Lett.*, vol. 13, no. 2, pp. 709–715, Feb. 2013, doi: 10.1021/nl304379k.
- [49] M. T. McDowell *et al.*, “In Situ TEM of Two-Phase Lithiation of Amorphous Silicon Nanospheres,” *Nano Lett.*, vol. 13, no. 2, pp. 758–764, Feb. 2013, doi: 10.1021/nl3044508.
- [50] V. Baranchugov, E. Markevich, E. Pollak, G. Salitra, and D. Aurbach, “Amorphous silicon thin films as a high capacity anodes for Li-ion batteries in ionic liquid electrolytes,” *Electrochem. commun.*, vol. 9, no. 4, pp. 796–800, Apr. 2007, doi: 10.1016/j.elecom.2006.11.014.
- [51] B. Key, M. Morcrette, J.-M. Tarascon, and C. P. Grey, “Pair Distribution Function Analysis and Solid State NMR Studies of Silicon Electrodes for Lithium Ion Batteries: Understanding the (De)lithiation Mechanisms,” *J. Am. Chem. Soc.*, vol. 133, no. 3, pp. 503–512, Jan. 2011, doi: 10.1021/ja108085d.
- [52] M. Rutttert, V. Siozios, M. Winter, and T. Placke, “Synthesis and Comparative Investigation of Silicon Transition Metal Silicide Composite Anodes for Lithium Ion Batteries,” *Zeitschrift für Anorg. und Allg. Chemie*, vol. 645, no. 3, pp. 248–256, Feb. 2019, doi: 10.1002/zaac.201800436.
- [53] M. Salah, P. Murphy, C. Hall, C. Francis, R. Kerr, and M. Fabretto, “Pure silicon thin-film anodes for lithium-ion batteries: A review,” *J. Power Sources*, vol. 414, no. November 2018, pp. 48–67, Feb. 2019, doi: 10.1016/j.jpowsour.2018.12.068.
- [54] J. Wu *et al.*, “Multilayered silicon embedded porous carbon/graphene hybrid film as a high performance anode,” *Carbon N. Y.*, vol. 84, no. 1, pp. 434–443, 2015, doi: 10.1016/j.carbon.2014.12.036.

- [55] H. Jia *et al.*, “Facile Synthesis and Lithium Storage Properties of a Porous NiSi₂/Si/Carbon Composite Anode Material for Lithium-Ion Batteries,” *ACS Appl. Mater. Interfaces*, vol. 7, no. 3, pp. 1508–1515, Jan. 2015, doi: 10.1021/am506486w.
- [56] Y. Horowitz, H. L. Han, P. N. Ross, and G. A. Somorjai, “In Situ Potentiodynamic Analysis of the Electrolyte/Silicon Electrodes Interface Reactions - A Sum Frequency Generation Vibrational Spectroscopy Study,” *J. Am. Chem. Soc.*, vol. 138, no. 3, pp. 726–729, 2016, doi: 10.1021/jacs.5b10333.
- [57] C. Pereira-Nabais *et al.*, “Interphase chemistry of Si electrodes used as anodes in Li-ion batteries,” *Appl. Surf. Sci.*, vol. 266, pp. 5–16, Feb. 2013, doi: 10.1016/j.apsusc.2012.10.165.
- [58] L.-F. Cui, R. Ruffo, C. K. Chan, H. Peng, and Y. Cui, “Crystalline-Amorphous Core-Shell Silicon Nanowires for High Capacity and High Current Battery Electrodes,” *Nano Lett.*, vol. 9, no. 1, pp. 491–495, Jan. 2009, doi: 10.1021/nl8036323.
- [59] B. Laïk, D. Ung, A. Caillard, C. S. Cojocaru, D. Pribat, and J. P. Pereira-Ramos, “An electrochemical and structural investigation of silicon nanowires as negative electrode for Li-ion batteries,” *J. Solid State Electrochem.*, vol. 14, no. 10, pp. 1835–1839, 2010, doi: 10.1007/s10008-010-1045-5.
- [60] I. Hasa *et al.*, “Electrochemical Reactivity and Passivation of Silicon Thin-Film Electrodes in Organic Carbonate Electrolytes,” *ACS Appl. Mater. Interfaces*, vol. 12, no. 36, pp. 40879–40890, Sep. 2020, doi: 10.1021/acsami.0c09384.
- [61] E. Pollak, G. Salitra, V. Baranchugov, and D. Aurbach, “In Situ Conductivity, Impedance Spectroscopy, and Ex Situ Raman Spectra of Amorphous Silicon during the Insertion/Extraction of Lithium,” *J. Phys. Chem. C*, vol. 111, no. 30, pp. 11437–11444, Aug. 2007, doi: 10.1021/jp0729563.

- [62] J. W. Smith *et al.*, “X-Ray absorption spectroscopy of LiBF₄ in propylene carbonate: a model lithium ion battery electrolyte,” *Phys. Chem. Chem. Phys.*, vol. 16, no. 43, pp. 23568–23575, 2014, doi: 10.1039/C4CP03240C.
- [63] J. W. Smith *et al.*, “X-Ray absorption spectroscopy of LiBF₄ in propylene carbonate: A model lithium ion battery electrolyte,” *Phys. Chem. Chem. Phys.*, vol. 16, no. 43, pp. 23568–23575, 2014, doi: 10.1039/c4cp03240c.
- [64] S. G. Urquhart and H. Ade, “Trends in the Carbonyl Core (C 1S, O 1S) → π^* C=O Transition in the Near-Edge X-ray Absorption Fine Structure Spectra of Organic Molecules,” *J. Phys. Chem. B*, vol. 106, no. 34, pp. 8531–8538, Aug. 2002, doi: 10.1021/jp0255379.
- [65] L. G. Parratt, C. F. Hempstead, and E. L. Jossem, “‘Thickness Effect’ in Absorption Spectra near Absorption Edges,” *Phys. Rev.*, vol. 105, no. 4, pp. 1228–1232, Feb. 1957, doi: 10.1103/PhysRev.105.1228.
- [66] G. S. Henderson, F. M. F. De Groot, and B. J. A. Moulton, “X-ray absorption near-edge structure (XANES) spectroscopy,” *Rev. Mineral. Geochemistry*, vol. 78, no. February, pp. 75–138, 2014, doi: 10.2138/rmg.2014.78.3.
- [67] S. L. M. Schroeder, G. D. Moggridge, E. Chabala, R. M. Ormerod, T. Rayment, and R. M. Lambert, “Possibilities and limitations of a new experimental technique,” *Faraday Discuss.*, vol. 105, no. 0, pp. 317–336, 1996.
- [68] D. M. Pease, “Thickness Effect in X-Ray Absorption Edges of Metals and Alloys.,” *Appl. Spectrosc.*, vol. 30, no. 4, pp. 405–410, 1976, doi: 10.1366/000370276774457056.
- [69] E. A. Stern and K. Kim, “Thickness effect on the extended-x-ray-absorption-fine-structure amplitude,” *Phys. Rev. B*, vol. 23, no. 8, pp. 3781–3787, 1981, doi: 10.1103/PhysRevB.23.3781.

- [70] T. Kachel, "The plane grating monochromator beamline U49-2 PGM-1 at BESSY II," *J. large-scale Res. Facil. JLSRF*, vol. 2, pp. 2–5, 2016, doi: 10.17815/jlsrf-2-75.
- [71] J. Stöhr, *NEXAFS Spectroscopy*, vol. 25, no. 9. Berlin, Heidelberg: Springer Berlin Heidelberg, 1992.
- [72] K. Kim, P. Zhu, N. Li, X. Ma, and Y. Chen, "Characterization of oxygen containing functional groups on carbon materials with oxygen K-edge X-ray absorption near edge structure spectroscopy," *Carbon N. Y.*, vol. 49, no. 5, pp. 1745–1751, Apr. 2011, doi: 10.1016/j.carbon.2010.12.060.
- [73] S. Han, "A salient effect of density on the dynamics of nonaqueous electrolytes," *Sci. Rep.*, vol. 7, no. April, pp. 1–9, 2017, doi: 10.1038/srep46718.
- [74] M. S. Ding, K. Xu, and T. R. Jow, "Liquid-Solid Phase Diagrams of Binary Carbonates for Lithium Batteries," *J. Electrochem. Soc.*, vol. 147, no. 5, p. 1688, 2000, doi: 10.1149/1.1393419.
- [75] F. Frati, M. O. J. Y. Hunault, and F. M. F. de Groot, "Oxygen K-edge X-ray Absorption Spectra," *Chem. Rev.*, vol. 120, no. 9, pp. 4056–4110, May 2020, doi: 10.1021/acs.chemrev.9b00439.
- [76] A. P. Hitchcock and C. E. Brion, "Inner-shell excitation of formaldehyde, acetaldehyde and acetone studied by electron impact," *J. Electron Spectros. Relat. Phenomena*, vol. 19, no. 2, pp. 231–250, 1980, doi: 10.1016/0368-2048(80)87006-X.
- [77] E. de Clermont Gallerande *et al.*, "Quantification of non-bridging oxygens in silicates using X-ray Raman scattering," *J. Non. Cryst. Solids*, vol. 528, pp. 1–27, 2020, doi: 10.1016/j.jnoncrysol.2019.119715.
- [78] M. J. Zachman, Z. Tu, S. Choudhury, L. A. Archer, and L. F. Kourkoutis, "Cryo-STEM

mapping of solid–liquid interfaces and dendrites in lithium-metal batteries,” *Nature*, vol. 560, no. 7718, pp. 345–349, 2018, doi: 10.1038/s41586-018-0397-3.

- [79] R. Qiao, Y.-D. Chuang, S. Yan, and W. Yang, “Soft X-Ray Irradiation Effects of Li₂O₂, Li₂CO₃ and Li₂O Revealed by Absorption Spectroscopy,” *PLoS One*, vol. 7, no. 11, p. e49182, Nov. 2012, doi: 10.1371/journal.pone.0049182.
- [80] S. Yang *et al.*, “Soft X-ray XANES studies of various phases related to LiFePO₄ based cathode materials,” *Energy Environ. Sci.*, vol. 5, no. 5, pp. 7007–7016, 2012, doi: 10.1039/c2ee03445j.
- [81] Y. He *et al.*, “Progressive growth of the solid–electrolyte interphase towards the Si anode interior causes capacity fading,” *Nat. Nanotechnol.*, Jul. 2021, doi: 10.1038/s41565-021-00947-8.
- [82] D. Aurbach, Y. Gofer, M. Ben-Zion, and P. Aped, “The behaviour of lithium electrodes in propylene and ethylene carbonate: The major factors that influence Li cycling efficiency,” *J. Electroanal. Chem.*, vol. 339, no. 1–2, pp. 451–471, 1992, doi: 10.1016/0022-0728(92)80467-l.
- [83] D. Aurbach, Y. Ein-Eli, O. Chusid (Youngman), Y. Carmeli, M. Babai, and H. Yamin, “The Correlation Between the Surface Chemistry and the Performance of Li-Carbon Intercalation Anodes for Rechargeable ‘Rocking-Chair’ Type Batteries,” *J. Electrochem. Soc.*, vol. 141, no. 3, pp. 603–611, 1994, doi: 10.1149/1.2054777.
- [84] K. Xu *et al.*, “Syntheses and characterization of lithium alkyl mono- and bicarbonates as components of surface films in Li-ion batteries,” *J. Phys. Chem. B*, vol. 110, no. 15, pp. 7708–7719, 2006, doi: 10.1021/jp0601522.
- [85] G. V. Zhuang, K. Xu, H. Yang, T. R. Jow, and P. N. Ross, “Lithium Ethylene Dicarboxate Identified as the Primary Product of Chemical and Electrochemical Reduction of EC in 1.2

- M LiPF₆/EC:EMC Electrolyte," *J. Phys. Chem. B*, vol. 109, no. 37, pp. 17567–17573, Sep. 2005, doi: 10.1021/jp052474w.
- [86] C. Cao *et al.*, "Solid Electrolyte Interphase on Native Oxide-Terminated Silicon Anodes for Li-Ion Batteries," *Joule*, vol. 3, no. 3, pp. 762–781, 2019, doi: 10.1016/j.joule.2018.12.013.
- [87] S. K. Heiskanen, J. Kim, and B. L. Lucht, "Generation and Evolution of the Solid Electrolyte Interphase of Lithium-Ion Batteries," *Joule*, vol. 3, no. 10, pp. 2322–2333, 2019, doi: 10.1016/j.joule.2019.08.018.
- [88] S. S. Harilal, J. P. Allain, A. Hassanein, M. R. Hendricks, and M. Nieto-Perez, "Reactivity of lithium exposed graphite surface," *Appl. Surf. Sci.*, vol. 255, no. 20, pp. 8539–8543, 2009, doi: 10.1016/j.apsusc.2009.06.009.
- [89] R. Qiao *et al.*, "Distinct Solid-Electrolyte-Interphases on Sn (100) and (001) Electrodes Studied by Soft X-Ray Spectroscopy," *Adv. Mater. Interfaces*, vol. 1, no. 3, pp. 1–6, 2014, doi: 10.1002/admi.201300115.
- [90] Q. Li *et al.*, "Identification of the Solid Electrolyte Interface on the Si/C Composite Anode with FEC as the Additive," *ACS Appl. Mater. Interfaces*, vol. 11, no. 15, pp. 14066–14075, 2019, doi: 10.1021/acsami.8b22221.
- [91] A. P. Hitchcock and C. E. Brion, "K-shell excitation of HF and F₂ studied by electron energy-loss spectroscopy," *J. Phys. B At. Mol. Phys.*, vol. 14, no. 22, pp. 4399–4413, 1981, doi: 10.1088/0022-3700/14/22/022.
- [92] M. B. Robin, I. Ishii, R. McLaren, and A. P. Hitchcock, "Fluorination effects on the inner-shell spectra of unsaturated molecules," *J. Electron Spectros. Relat. Phenomena*, vol. 47, no. C, pp. 53–92, 1988, doi: 10.1016/0368-2048(88)85005-9.
- [93] S. Y. Turishchev *et al.*, "Surface deep profile synchrotron studies of mechanically modified

- top-down silicon nanowires array using ultrasoft X-ray absorption near edge structure spectroscopy,” *Sci. Rep.*, vol. 9, no. 1, pp. 1–7, 2019, doi: 10.1038/s41598-019-44555-y.
- [94] P. E. Batson, K. L. Kavanagh, C. Y. Wong, and J. M. Woodall, “Local bonding and electronic structure obtained from electron energy loss scattering,” *Ultramicroscopy*, vol. 22, no. 1–4, pp. 89–101, 1987, doi: 10.1016/0304-3991(87)90053-2.
- [95] J. Yang, N. Solomatin, A. Kraytsberg, and Y. Ein-Eli, “In-Situ Spectro-electrochemical Insight Revealing Distinctive Silicon Anode Solid Electrolyte Interphase Formation in a Lithium-ion Battery,” *ChemistrySelect*, vol. 1, no. 3, pp. 572–576, Mar. 2016, doi: 10.1002/slct.201600119.
- [96] B. T. Young, D. R. Heskett, C. C. Nguyen, M. Nie, J. C. Woicik, and B. L. Lucht, “Hard X-ray Photoelectron Spectroscopy (HAXPES) Investigation of the Silicon Solid Electrolyte Interphase (SEI) in Lithium-Ion Batteries,” *ACS Appl. Mater. Interfaces*, vol. 7, no. 36, pp. 20004–20011, Sep. 2015, doi: 10.1021/acsami.5b04845.
- [97] G. M. Veith *et al.*, “Direct Determination of Solid-Electrolyte Interphase Thickness and Composition as a Function of State of Charge on a Silicon Anode,” *J. Phys. Chem. C*, vol. 119, no. 35, pp. 20339–20349, Sep. 2015, doi: 10.1021/acs.jpcc.5b06817.
- [98] S. J. An, J. Li, C. Daniel, D. Mohanty, S. Nagpure, and D. L. Wood, “The state of understanding of the lithium-ion-battery graphite solid electrolyte interphase (SEI) and its relationship to formation cycling,” *Carbon N. Y.*, vol. 105, pp. 52–76, Aug. 2016, doi: 10.1016/j.carbon.2016.04.008.
- [99] R. Seidel, M. N. Pohl, H. Ali, B. Winter, and E. F. Aziz, “Advances in liquid phase soft-x-ray photoemission spectroscopy: A new experimental setup at BESSY II,” *Rev. Sci. Instrum.*, vol. 88, no. 7, 2017, doi: 10.1063/1.4990797.
- [100] E. F. Aziz, J. Xiao, R. Golnak, and M. Tesch, “LiXEdrom: High Energy Resolution RIXS

Station dedicated to Liquid Investigation at BESSY II,” *J. large-scale Res. Facil. JLSRF*, vol. 2, pp. 1–4, 2016, doi: 10.17815/jlsrf-2-85.

- [101] A. Balzer, M. Witt, E. Suljoti, and E. Schierle, “Status of the Continuous Mode Scan for Undulator Beamlines at BESSY II,” *Proc. 15th Int. Conf. Accel. Large Exp. Phys. Control Syst.*, vol. JACOW, 201, pp. 1091–1095, 2015, [Online]. Available: <http://icalepcs2015.vrws.de/papers/thha3o02.pdf>.